

# Probing Non-Equilibrium Topological Order on a Quantum Processor

Out-of-equilibrium phases in many-body systems constitute a new paradigm in quantum matter—they exhibit dynamical properties that may otherwise be forbidden by equilibrium thermodynamics. Among these non-equilibrium phases are periodically driven (Floquet) systems [1–5], that are generically difficult to simulate classically due to their high entanglement. Using an array of superconducting qubits, we realize a Floquet topologically ordered state theoretically proposed in Ref. [6], image the characteristic dynamics of its chiral edge modes, and characterize its emergent anyonic excitations. Devising an interferometric algorithm allows us to introduce and measure a bulk topological invariant to probe the dynamical transmutation of anyons for system sizes up to 58 qubits. Our work demonstrates that quantum processors can provide key insights into the thus-far largely unexplored landscape of highly entangled non-equilibrium phases of matter.

M. Will<sup>1,2,‡</sup>, T. A. Cochran<sup>3,‡</sup>, E. Rosenberg<sup>4</sup>, B. Jobst<sup>1,2</sup>, N. M. Eassa<sup>4,5</sup>, P. Roushan<sup>4,§</sup>, M. Knap<sup>1,2,§</sup>, A. Gammon-Smith<sup>6,7,§</sup>, F. Pollmann<sup>1,2,§</sup>,

<sup>1</sup> Technical University of Munich, TUM School of Natural Sciences, Physics Department, 85748 Garching, Germany

<sup>2</sup> Munich Center for Quantum Science and Technology (MCQST), Schellingstr. 4, 80799 München, Germany

<sup>3</sup> Department of Physics, Princeton University, Princeton, NJ, USA

<sup>4</sup> Google Research, Mountain View, CA, USA

<sup>5</sup> Department of Physics and Astronomy, Purdue University, West Lafayette, IN 47906, USA

<sup>6</sup> School of Physics and Astronomy, University of Nottingham, Nottingham, NG7 2RD, UK

<sup>7</sup> Centre for the Mathematics and Theoretical Physics of Quantum Non-Equilibrium Systems, University of Nottingham, Nottingham, NG7 2RD, UK

<sup>‡</sup> These authors contributed equally to this work.

<sup>§</sup> Corresponding authors: pedramr@google.com, michael.knap@ph.tum.de, Adam.Gammon-Smith@nottingham.ac.uk, frank.pollmann@tum.de

Quantum many-body systems display a rich landscape of equilibrium phases of matter. Among them are symmetry breaking phases and topological phases [7–9]. While the former are described by local order parameters, the latter are instead characterized by their non-local entanglement [10, 11] and the emergence of fractionalized anyonic excitations [12–14]. The non-local nature of states with topological order is the underlying principle leveraged in many quantum error correcting codes [15], in which quantum information is encoded in locally indistinguishable ground states that are robust to local perturbations. Recent experimental advances allow the realization of such topological states on quantum processors, through scalable quantum circuits [16–20].

Remarkably, it has been predicted early on that time-periodic driving can lead to the emergence of topologically protected non-equilibrium phases of matter that are fundamentally distinct from those in thermal equilibrium [21]. A recently proposed example in two-dimensional systems shows that periodically driving non-interacting particles can support robust chiral edge states, even when the Chern numbers of all bulk bands are zero—a property forbidden in static band structures [1–3, 22, 23]. Moreover, discrete time crystals [4, 5, 24–30] can be realized in driven systems, which, crucially, cannot be stabilized in any equilibrium scenario [31–33]. Their prediction and subsequent realization [26–30] brought spatio-temporal ordering to focus and motivated further exploration of symmetry-protected non-equilibrium phases of matter [34, 35] as well as topologically ordered time crystals [36, 37].

This leads to a central question: Can novel types of topological order be realized away from equilibrium and by time-periodic driving? Theoretical studies propose the Floquet Kitaev model as a paragon [6, 38]; a periodically driven version of Kitaev’s honeycomb model [39]. Under strong driving, this system has been predicted to exhibit *Floquet topological order (FTO)* [6] and time-vortex excitations [40].

Here, we implement efficient quantum circuits in a two-dimensional lattice of superconducting qubits and probe two key non-equilibrium signatures of the Floquet topologically ordered phase. The first is the presence of topologically protected chiral edge modes hosting non-abelian Majorana modes. Importantly, these edge modes occur with zero Chern number for the bulk bands [6]. This is in sharp contrast to the equilibrium setting where a non-zero integer value of this topological invariant is a requisite for the existence of chiral modes. The second distinguishing signature is the non-equilibrium topological order in the bulk of the system. Unique to this Floquet setting are two distinct anyon types transmuting between each other, alternating with twice the period of the drive. Quantum processors allow us to adjust parameters away from the analytically tractable regimes of the Floquet Kitaev model and examine the stability of FTO for different parameter regimes. These are regimes in which, due to the rapid generation of entanglement, the simulation capabilities of classical computers are strongly limited. Quantum processors further allow us to design protocols for measuring observables that unambiguously relate to the underlying physics.

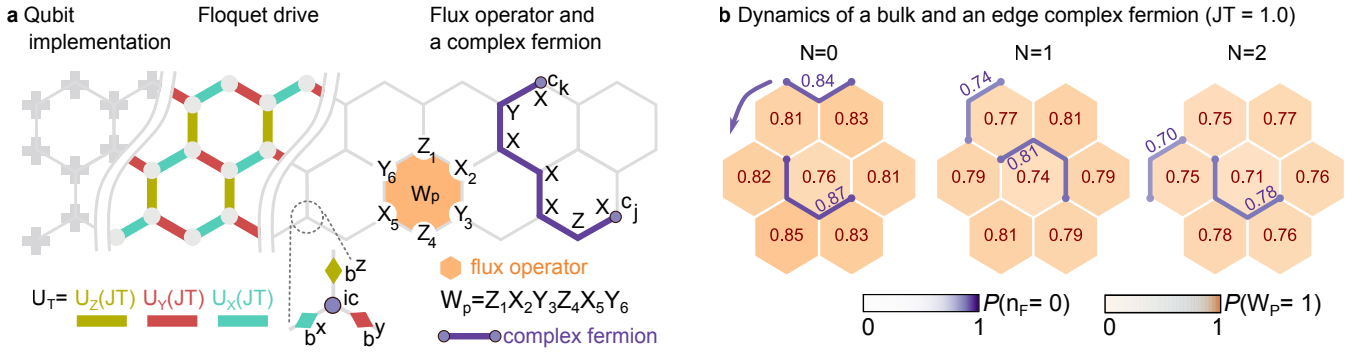


FIG. 1. **Realization of the Floquet Kitaev model.** **a** The hexagonal lattice can readily be embedded on the square lattice geometry of the superconducting qubits. Stroboscopic time evolution realizes the Floquet Kitaev model, where colored bonds correspond to the direction-dependent couplings. On each site, the qubit can be mapped to four Majorana operators  $b^x, b^y, b^z$  and  $c$ . A plaquette operator  $W_P$ , which is a Pauli string around the hexagons of the lattice, is highlighted. Pairing two  $c$ -Majoranas together results in a complex fermion shown in purple, and its occupation number operator is given by the indicated Pauli string. **b** Measurements for fluxes and paired emergent Majorana modes with occupation  $n_F = 0$ , during the stroboscopic time evolution. Here we specifically track one fermion occupation along the edge and one in the bulk (other fermions are not shown for clarity) for up to  $N = 2$  cycles. Data taken with dynamical decoupling and randomized compiling for CZ gates ( $N_{\text{twirling}} = 20$ ,  $N_{\text{shots}} = 10^6$ , 26 qubits).

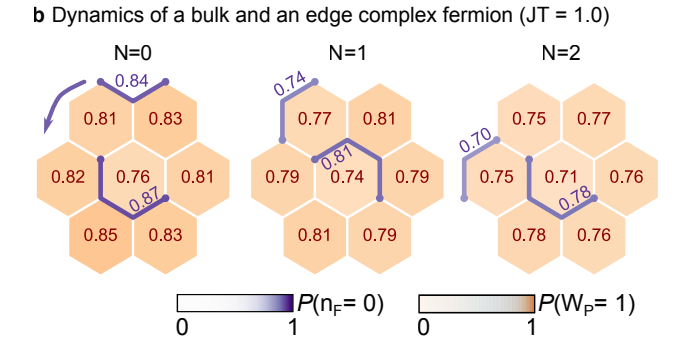
### Realizing the Floquet Kitaev Model

The Floquet Kitaev model, introduced in Ref. [6], is a periodically driven analogue of Kitaev's honeycomb model [39]. In much the same way that Kitaev's honeycomb model is the archetype for quantum spin-liquids in equilibrium, the Floquet Kitaev model provides an exactly solvable model for FTO. It consists of spin-1/2 degrees of freedom arranged on the vertices of a honeycomb lattice as illustrated in Fig. 1a. The three types of bonds are labeled by  $x, y$ , and  $z$ , indicating the type of direction-dependent Ising coupling applied on that bond. We implement the stroboscopic evolution given by

$$U_T = U_Z(JT) U_Y(JT) U_X(JT) \quad (1)$$

where  $U_\alpha(JT) = \exp\{-i\frac{\pi}{4}JT \sum_{\langle j,k \rangle_\alpha} \alpha_j \alpha_k\}$ , with Pauli operators  $\alpha \in \{X, Y, Z\}$ . The sums run over all neighboring  $j, k$  spin pairs of the corresponding bond type. The dynamics are controlled by  $JT$ , where  $J$  is the coupling parameter and  $T$  the driving period. We implement the  $U_\alpha$  driving terms with single qubit rotations and two-qubit C-PHASE gates (details in SI [41]). Depending on the strength of the driving, the model is in one of several non-equilibrium phases [6]. The FTO phase, as a distinct non-equilibrium phase of matter, is predicted to exist close to  $JT = 1$  even away from the integrable case [6].

The Floquet Kitaev model is well understood due to a Majorana representation of the spins, which reveals the free-fermion solvability of the model [6, 38]. On each site, four Majorana operators  $\{c, b^x, b^y, b^z\}$  are defined as shown in Fig. 1a, such that the Pauli operators are  $\alpha_j = ic_j b_j^\alpha$ . This representation enlarges the Hilbert space, and the physical states  $|\psi\rangle$  are those with  $c_j b_j^x b_j^y b_j^z |\psi\rangle = |\psi\rangle$  for all  $j$ . The Floquet Kitaev model



has a set of conserved quantities  $u_{jk} = ib_j^\alpha b_k^\alpha$ , where  $\alpha$  is the Pauli operator associated with the bond  $\langle j, k \rangle$ . Products of the operators  $u_{jk}$  around the hexagonal plaquettes  $P$  as shown in Fig. 1a correspond to  $\mathbb{Z}_2$  gauge-invariant conserved quantities,

$$W_P = \prod_{\langle j,k \rangle \in \partial P} u_{jk}, \quad (2)$$

where we refer to  $W_P = +1$  as flux-free. Using the Majorana representation, the driving terms are then given by  $U_\alpha(JT) = \exp\{-JT\frac{\pi}{4} \sum_{\langle j,k \rangle_\alpha} u_{jk} c_j c_k\}$ , which are quadratic in the  $c_i$ -Majorana fermion operators. These terms correspond to hopping operators for the  $c$ -fermions, and perform a Majorana swap when  $JT = 1$ . To monitor the dynamics of the emergent Majorana excitations, we define measurable density operators of a complex fermion  $\psi$  resulting from pairing two  $c$ -Majoranas at sites  $j$  and  $k$ ,

$$n_F(j, k) = (i\phi_{jk} c_j c_k + 1)/2, \quad \text{with } \phi_{jk} = \prod_{\langle l,m \rangle \in \Gamma} u_{lm}, \quad (3)$$

and  $\Gamma$  is a path connecting those sites. By including the string  $\phi_{jk}$ , this density operator can be equivalently written as a Pauli string and thus be directly measured on the quantum processor (see SI [41] for details).

By stroboscopic measurements, we visualize the dynamics of the paired Majoranas in the FTO phase. For this we first implement a unitary circuit  $U_{\text{FF}}$  to prepare the system in a flux-free (FF) state,

$$|\Psi_{\text{FF}}\rangle = U_{\text{FF}} |0\rangle^{\otimes N}, \quad \text{with } W_P |\Psi_{\text{FF}}\rangle = |\Psi_{\text{FF}}\rangle \forall P. \quad (4)$$

This is achieved by noting the relationship to the ground states of the toric code, which can be prepared efficiently

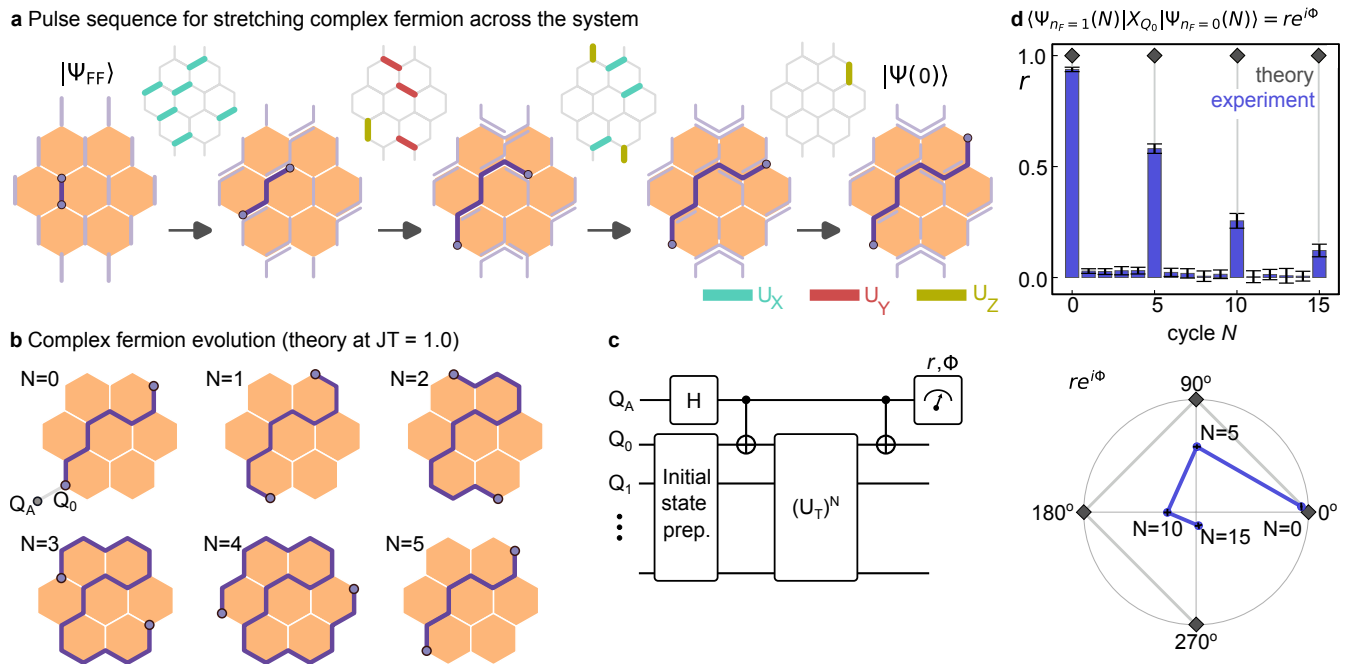


FIG. 2. **Dynamical Majorana edge mode interferometry.** **a** Gate sequence on top of the flux-free state  $|\Psi_{FF}\rangle$  to pair Majorana modes on opposite sides of the system. **b** Transformation of the stretched, complex fermion under Floquet driving. For clarity other fermions are not shown. **c** Circuit for the Hadamard test to measure the overlap between evolved states with the fermion occupied and unoccupied, respectively, in order to extract the relative phase of  $e^{i\pi/2}$ . **d** Radial component of the overlap, comparing data taken on the device with theory. Polar plot of the complex value of the overlap shown at multiples of  $N = 5$  cycles. Data taken with dynamical decoupling, randomized compiling, and post selection of the flux through each plaquette of the outer ring, see SI [41] ( $N_{\text{twirling}} = 20, N_{\text{shots}} = 5 \times 10^5$ , 27 qubits). Error bars indicate the standard error of the mean, for details see SI [41].

with unitary circuits with a depth linear in the width of the system [16, 42]. The preparation also fixes a unique pairing of Majoranas into complex fermions with  $n_F = 0$  on neighbouring sites on the  $z$ -bonds (not shown here, but in SI [41]). Using a sequence of bond operators of the form  $\exp\{-\frac{\pi}{4}u_{jk}c_jc_k\}$ , the Majoranas are swapped until the state  $|\Psi(0)\rangle$  with the desired pairing of Majoranas is reached (which can be non-local). The state  $|\Psi(0)\rangle$  is then the initial state for the subsequent evolution with the Floquet unitary  $U_T$ . Figure 1b shows the measured fluxes  $W_P$  and the dynamics of two selected densities  $n_F(j, k)$  of paired Majoranas following the Floquet evolution with  $JT = 1$ . The bulk Majoranas form closed orbits of period two and the chiral motion of the fermions along the edge is clearly visible—resembling the (skipping) cyclotron orbits in the semi-classical picture of quantum Hall physics. The experimental data demonstrates an approximate conservation of the plaquette fluxes  $W_P$  and densities up to noise that accumulates with circuit depth.

### Chiral Majorana Edge Mode Interferometry

We next reveal the non-trivial exchange statistics of the Majorana edge modes. The exchange of a pair of Majorana excitations results in the accumulation of a phase

that depends on the fermion parity of the pair. More precisely, if the pair of Majorana excitations corresponds to an occupied fermionic state  $\langle n_F \rangle = 1$ , then exchange will lead to a phase factor of  $e^{-i\pi/4}$ , whereas an unoccupied fermion  $\langle n_F \rangle = 0$  gives  $e^{i\pi/4}$ . To extract this topological phase information experimentally, we first prepare  $|\Psi_{FF}\rangle$  and then modify it to  $|\Psi(0)\rangle$ , which has a Majorana pair stretched across the system as depicted in Fig. 2a. For the chosen setup, the occupancy can be changed by acting with a Pauli  $X$  on qubit 0. The Floquet driving drags the modes around the edge of the system until the Majoranas are exchanged after a system-size dependent number of time steps and returned to an equivalent configuration, as shown in Fig. 2b.

Similar to a Hadamard test using an ancilla qubit, we devised a pulse sequence which allows us to measure the—otherwise global—relative phase accumulation by the quantum states. Depicted in Fig. 2c, the key element is a controlled operation which enables the parallel evolution of an occupied and an unoccupied Majorana pair and maps the relative phase of the two states to the ancilla qubit ( $Q_A$ ). We compare the two occupancies for the non-local pair of Majoranas, which enables us to read off the amplitude  $r$  and phase  $\phi$  of this overlap. The overlap shows revivals with period  $N = 5$ , shown in

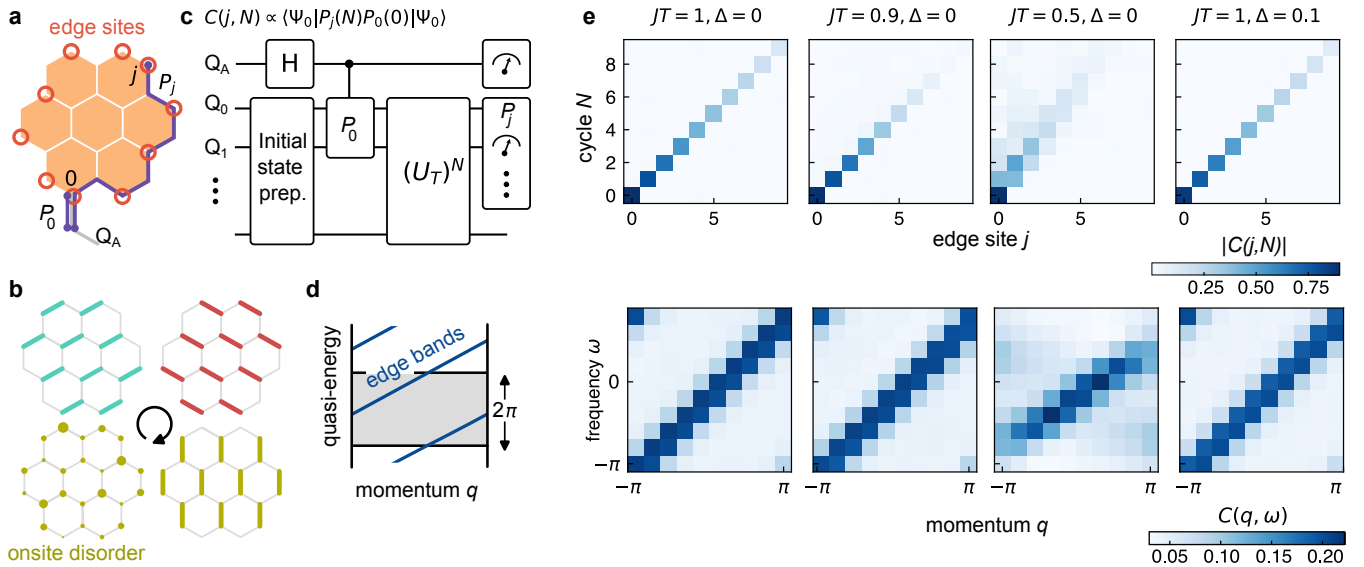


FIG. 3. **Majorana edge mode spectrum.** **a** The hexagonal lattice with edge sites shown in red. We also indicate the Pauli strings corresponding to the fermion occupation for two of the sites on the edge. **b** Addition of a fourth time step with a random on-site  $Z$ -field that breaks integrability is given by  $U_{\text{disorder}} = e^{-iJT\pi/4 \sum_i h_i Z_i}$  with  $h_i \in [-\Delta, \Delta]$ . **c** Schematic of the circuit to measure the unequal-time Pauli-string correlator, which is equivalent to the real-space Majorana spectral function, see text for more details. **d** Exemplary sketch of spectrum in FTO phase. Edge states are shown in blue. **e** First row: Spectral function in real space for  $\Delta = 0$  and varying values of  $JT$  (first three columns), and for  $JT = 1, \Delta = 0.1$  (last column), where the data is averaged over  $N_{\text{av}} = 20$  disorder configurations. Second row: Fourier transformed data. Data taken with dynamical decoupling, randomized compiling for CZ gates, and post selection on middle plaquette in experiments without disordered field (first three columns), see SI [41] ( $N_{\text{twirling}} = 20, N_{\text{shots}} = 5 \times 10^5, 27$  qubits).

Fig. 2d, matching the period of exchange for the highlighted pair of Majoranas for the considered geometry in Fig. 2b. Compared to the theoretically expected value  $r = 1$  for the amplitudes of the revivals, we observe decay due to errors and decoherence on the processor. For intermediate time steps, the final controlled operation does not simply flip the fermion occupation, and thus creates an orthogonal state for which the overlap is zero as expected. By measuring the real and imaginary part of the overlap, we observe a relative phase of  $e^{i\pi/2}$  at multiples of the period of  $N = 5$  which demonstrates that the Majorana modes at the edge are dynamically exchanged. While the measured amplitude shows significant decay, we find the measured complex phase to be remarkably stable.

### Spectroscopy of Edge Modes

Thus far we have focused on the analytically solvable fixed point circuit by setting  $JT = 1$ . The FTO is, however, an extended non-equilibrium phase of matter [6]. Now we probe the robustness of the edge modes and image the spectrum by measuring the two-time Majorana spectral function along the edge of the system. The Fourier transform of this function reveals the momentum and quasi-energy resolved spectrum of the chiral edge mode. This spectral function is not directly measurable as it involves individual Majorana operators at a given

time, which are not accessible. However, we can augment the system by an additional qubit (protruding bond in Fig. 3a) that is not participating in the time evolution but instead is used to pair with the desired Majorana mode. The information of the edge mode can then be equivalently measured with unequal time correlators of Pauli strings

$$C(j, N) \propto \langle \psi_0 | P_j(N) P_0(0) | \psi_0 \rangle, \quad (5)$$

where  $P_j(N)$  is the corresponding Pauli string tracing the edge fermions evolved under  $N$  Floquet cycles. As written, this quantity would correspond to a four-point Majorana correlator. However, the modes on the undriven additional qubit cancel, leaving the sought-after equivalent two-point unequal time Majorana correlator (see SI [41]). Similar to the last pulse sequence, we use a Hadamard test to measure this unequal time Pauli correlator, as shown in Fig. 3c. To additionally probe the robustness of the edge modes, we move away from the fixed point  $JT = 1$  in two ways. We first detune the driving from this point by considering  $JT \neq 1$ . We also modify the drive sequence by adding a disordered  $Z$ -field as a fourth step in the stroboscopic evolution depicted in Fig. 3b and given by

$$U_{\text{disorder}} = e^{-iJT\pi/4 \sum_i h_i Z_i} \quad (6)$$

with  $h_i \in [-\Delta, \Delta]$ . This term explicitly breaks the integrability of the model by introducing dynamics to the

fluxes  $W_P$ .

In the FTO phase,  $JT = 1$  and  $JT = 0.9$ , the chiral edge mode is clearly visible in the energy-momentum resolved spectral function (lower panels in Fig. 3e). Tuning away from the fixed point has the effect of a very weak broadening corresponding to a decay of the mode, which is best visible in the real-space data, top panels in Fig. 3e. This decay is expected because we are measuring the spectral function on the edge sites only, and the edge modes are not solely supported on these sites away from  $JT = 1$ . The observed decay at  $JT = 1$  is due to the combination of coherent errors and decoherence in the device. Importantly, we observe the non-trivial winding of the mode in quasi-energy that is unique to this non-equilibrium phase. Furthermore, moving to the non-abelian Kitaev phase,  $JT = 0.5$ , we observe a qualitative difference in the dispersion of the chiral mode. In particular, there is no clear winding in quasi-energy, supporting that this regime is connected to the equilibrium phase. This is also visible in the real space data, which shows how the mode quickly dissolves into the bulk. The introduction of the disordered field has a remarkably weak effect on the chiral mode for the experimentally accessible time scales. Although disorder in the interacting model is not expected to result in many-body localization in the thermodynamic limit [43], we anticipate the existence of an extended pre-thermal regime, during which the phase remains protected from heating [44–48].

### Bulk Non-Equilibrium Topological Order

The second distinguishing signature of the FTO phase is the bulk non-equilibrium topological order characterized by the transmutation of anyon types [6, 38]. We use this unique phenomenology of the driven system to introduce an order parameter for the FTO phase. This order parameter is a topological invariant which oscillates between  $+1$  and  $-1$  in the FTO phase with twice the driving period, and is constant in the non-abelian Kitaev phase. In the bulk, the FTO phase is characterized by  $\mathbb{Z}_2$  topological order, and the associated  $e, m$  and  $\psi = e \times m$  anyons [6]. The  $m$  anyons correspond to flux defects ( $W_P = -1$ ),  $\psi$  is an occupied complex fermion ( $n_F = 1$ ) introduced above, and the  $e$  anyon is then the combination of a flux defect and an occupied fermion on a given plaquette (Fig. 4a). Since the fermion parity  $P_F = (-1)^{n_F} = \pm 1$  time evolves at the fixed point  $JT = 1$  as

$$U_T^\dagger P_F U_T = W_P P_F, \quad (7)$$

the fermion occupation remains constant during time evolution on a flux-free plaquette with  $W_P = 1$ . However, if the flux is  $W_P = -1$ , the fermion occupation will flip after each driving cycle, resulting in a periodicity of  $N = 2$ .

This transmutation of  $e \leftrightarrow m$  anyons is a key characteristic of this non-equilibrium topological order, and can

thus be referred to as an anyonic time crystal [6, 36, 37]. To probe this transmutation, we create an  $e$  anyon in the central plaquette of the system and move the paired  $e$  anyon to the boundary of the system, as shown in Fig. 4b. After evolving the system under the Floquet driving, we measure an electric loop operator  $O$  encircling this central plaquette, shown in Fig. 4a in green. This loop operator corresponds to creating a pair of electric anyons, dragging one around the loop, and then annihilating the pair, and can be measured as a Pauli expectation value. To define an invariant, we compute the ratio of this quantity and the loop measurement without an anyon at the center, in spirit of the Fredenhagen-Marcu equilibrium order parameter [49],

$$\eta(N) = \frac{\langle \Psi_e | O(N) | \Psi_e \rangle}{\langle \Psi_0 | O(N) | \Psi_0 \rangle}, \quad (8)$$

where  $O(N) = (U_T^\dagger)^N O (U_T)^N$ . In the thermodynamic limit, and the limit of large loop diameter, this defines a bulk invariant for the phase which oscillates between  $+1$  ( $e$  anyon) and  $-1$  ( $m$  anyon) in the FTO phase.

Experimentally realizing a phase requires showing that its signatures survive over a pre-thermal time scale when perturbed away from the fine-tuned points in parameter space, i.e. away from  $JT = 1$ , where the drive sequence corresponds to a Clifford circuit. The oscillations with period  $N = 2$  are clearly seen in the measured order parameter  $\eta(N)$  for different values of  $JT$  in the FTO phase; Fig. 4c. Since  $\eta(N)$  is estimated from a finite number of measurements, we regularize the denominator to account for shot noise SI [41]. By contrast, in the non-abelian Kitaev phase the oscillations are absent. This quantity is expected to be constant and equal to  $+1$  in the thermodynamic limit, but this is not observed because of the finite size. Adding the small disordered field, we further probe the robustness of the FTO phase in Fig. 4c. Our data is remarkably robust to increasing disorder strength. In the FTO phase the Fourier transform of the order parameter peaks at  $\pi$ , whereas in the Kitaev phase at zero, see sketch Fig. 4d. The difference  $|\eta((\omega = \pi))| - |\eta((\omega = 0))|$  is thus positive in the FTO phase and negative in the Kitaev phase. Tuning  $JT$  and  $\Delta$  we map out a pre-thermal non-equilibrium phase diagram in Fig. 4e.

### Outlook

The landscape of non-equilibrium phases of matter is largely unexplored thus far. Digital quantum processors provide an ideal platform to reveal the highly-entangled dynamical phases therein. The non-equilibrium topological order that we have probed in this work encapsulates a fundamentally unique phenomenology that is forbidden in thermal equilibrium. While many equilibrium phases are known and theoretically understood, the prospects for non-equilibrium phases of matter are still largely open. New order parameters, possibly akin to our

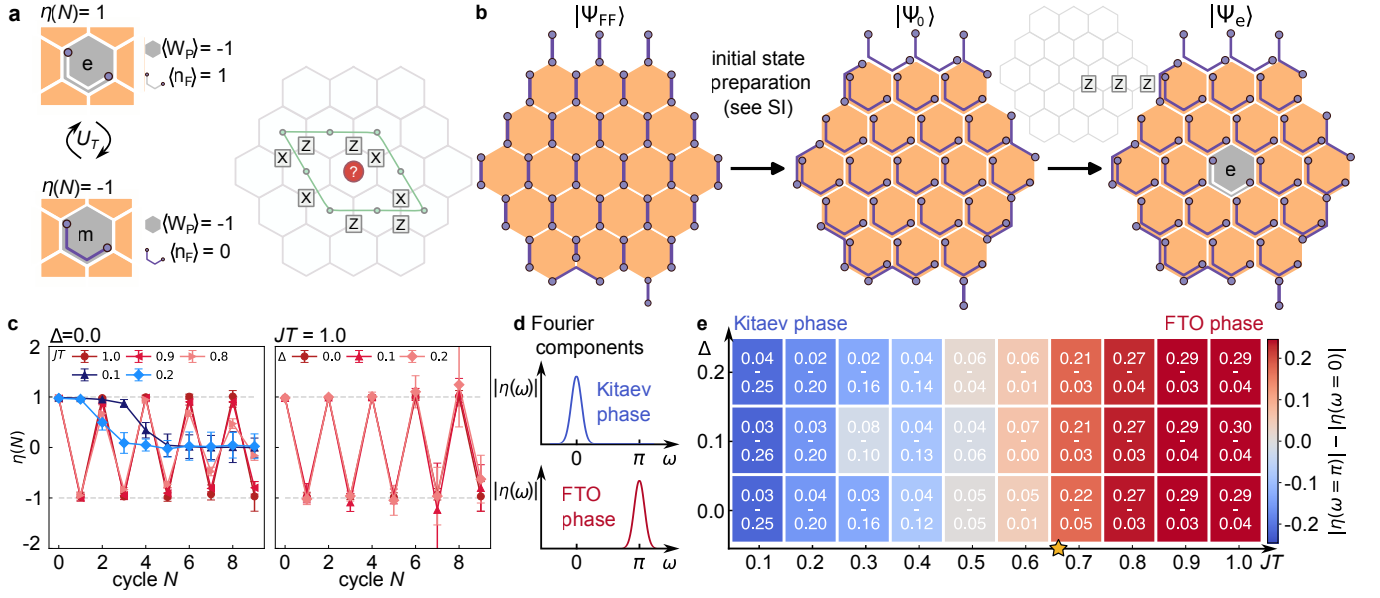


FIG. 4. **Bulk non-equilibrium topological order.** **a** Sketch of anyonic  $e$  and  $m$  anyons, which are transmuted in the bulk under the Floquet driving. Measuring the electric loop operator gives a negative or positive sign, for the  $e$  and  $m$  anyons, respectively. **b** Initial state preparation. Starting from the flux-free state  $|\Psi_{FF}\rangle$  we rearrange the fermions to prepare the state  $|\Psi_0\rangle$ . Applying three  $Z$  operators creates an  $e$  anyon in the center of the system yielding  $|\Psi_e\rangle$ . The paired anyon is pushed out of the system on the right hand side. **c** Bulk invariant showing oscillations in the FTO phase (red), which are absent in the Kitaev phase (blue). Oscillations in the invariant are robust to integrability breaking disorder on the time scale of the experiments. **d** In the Kitaev phase, the Fourier transform of the order parameter  $\eta(\omega)$  is expected to peak at zero frequency, whereas it peaks at  $\pi$  in the FTO phase. **e** Phase diagram as a function of the detuning  $JT$  and disorder  $\Delta$  obtained from the difference of the Fourier components at  $\pi$  (top number) and  $0$  (bottom number). The yellow star marks the critical point of the exactly solvable model ( $\Delta = 0$ ). Data taken with dynamical decoupling and randomized compiling for CZ gates ( $N_{\text{twirling}} = 20$ ,  $N_{\text{shots}} = 10^6$ ,  $N_{\text{disorder}} = 20$ , 58 qubits).

non-equilibrium loop order parameter, need to be developed to characterize these dynamical phases of matter. Our interferometric probes for imaging the dynamical transmutation of anyons provide a novel approach toward exploring highly entangled non-equilibrium phases of matter.

While completing this project, we became aware of related research that investigates the equilibrium Kitaev phase and its associated emergent fermionic dynamics, implemented on a neutral-atom quantum computing platform [50].

### Acknowledgments

M.W. thanks Ashvin Vishwanath and Erez Berg for helpful discussions. A.G-S. acknowledges support from the Royal Commission for the Exhibition of 1851, and support from the UK Research and Innovation (UKRI) under the UK government’s Horizon Europe funding guarantee [grant number EP/Y036069/1]. M.W., F.P., and M.K. acknowledge support from the Deutsche Forschungsgemeinschaft (DFG, German Research Foundation) under Germany’s Excellence Strategy—EXC—2111—390814868, TRR 360 – 492547816 and DFG grants

No. KN1254/1-2, KN1254/2-1, the European Research Council (ERC) under the European Union’s Horizon 2020 research and innovation programme (grant agreement No. 851161 and No. 771537), as well as the Munich Quantum Valley, which is supported by the Bavarian state government with funds from the Hightech Agenda Bayern Plus. M.W. and F.P. acknowledge support from the DFG Research Unit FOR 5522 (project-id 499180199). All experiments were conducted remotely on 72-qubit Google Sycamore (Figs. 1–3) and Willow (Fig. 4) processors [51, 52], with access provided via the Google Cloud Quantum Engine. Calibration and support were provided by the Quantum Hardware Residency Program. We thank the Google Quantum AI team for providing the quantum systems and support that enabled these results. The views expressed in this work are solely those of the authors and do not reflect the policy of Google or the Google Quantum AI team.

### Data and materials availability

Data and codes are available on Zenodo upon reasonable request [53].

- 
- [1] T. Kitagawa, E. Berg, M. Rudner, and E. Demler, Topological characterization of periodically driven quantum systems, *Phys. Rev. B* **82**, 235114 (2010).
- [2] M. S. Rudner, N. H. Lindner, E. Berg, and M. Levin, Anomalous edge states and the bulk-edge correspondence for periodically driven two-dimensional systems, *Phys. Rev. X* **3**, 031005 (2013).
- [3] R. Roy and F. Harper, Periodic table for floquet topological insulators, *Phys. Rev. B* **96**, 155118 (2017).
- [4] V. Khemani, A. Lazarides, R. Moessner, and S. L. Sondhi, Phase structure of driven quantum systems, *Phys. Rev. Lett.* **116**, 250401 (2016).
- [5] D. V. Else, B. Bauer, and C. Nayak, Floquet time crystals, *Phys. Rev. Lett.* **117**, 090402 (2016).
- [6] H. C. Po, L. Fidkowski, A. Vishwanath, and A. C. Potter, Radical chiral Floquet phases in a periodically driven Kitaev model and beyond, *Phys. Rev. B* **96**, 245116 (2017).
- [7] D. C. Tsui, H. L. Stormer, and A. C. Gossard, Two-dimensional magnetotransport in the extreme quantum limit, *Phys. Rev. Lett.* **48**, 1559 (1982).
- [8] R. B. Laughlin, Anomalous quantum Hall effect: An incompressible quantum fluid with fractionally charged excitations, *Phys. Rev. Lett.* **50**, 1395 (1983).
- [9] X. G. Wen and Q. Niu, Ground-state degeneracy of the fractional quantum hall states in the presence of a random potential and on high-genus Riemann surfaces, *Phys. Rev. B* **41**, 9377 (1990).
- [10] A. Kitaev and J. Preskill, Topological entanglement entropy, *Phys. Rev. Lett.* **96**, 110404 (2006).
- [11] M. Levin and X.-G. Wen, Detecting topological order in a ground state wave function, *Phys. Rev. Lett.* **96**, 110405 (2006).
- [12] J. M. Leinaas and J. Myrheim, On the theory of identical particles, *Il Nuovo Cimento B* **37**, 1 (1977).
- [13] F. Wilczek, Quantum mechanics of fractional-spin particles, *Phys. Rev. Lett.* **49**, 957 (1982).
- [14] C. Nayak, S. H. Simon, A. Stern, M. Freedman, and S. Das Sarma, Non-abelian anyons and topological quantum computation, *Rev. Mod. Phys.* **80**, 1083 (2008).
- [15] A. Kitaev, Fault-tolerant quantum computation by anyons, *Annals of Physics* **303**, 2 (2003).
- [16] K. J. Satzinger *et al.*, Realizing topologically ordered states on a quantum processor, *Science* **374**, 1237 (2021).
- [17] Y.-J. Liu, K. Shtengel, A. Smith, and F. Pollmann, Methods for simulating string-net states and anyons on a digital quantum computer, *PRX Quantum* **3**, 040315 (2022).
- [18] T. I. Andersen *et al.*, Non-abelian braiding of graph vertices in a superconducting processor, *Nature* **618**, 264 (2023).
- [19] M. Iqbal, N. Tantivasadakarn, R. Verresen, S. L. Campbell, J. M. Dreiling, C. Figgatt, J. P. Gaebler, J. Johansen, M. Mills, S. A. Moses, J. M. Pino, A. Ransford, M. Rowe, P. Siegfried, R. P. Stutz, M. Foss-Feig, A. Vishwanath, and H. Dreyer, Non-abelian topological order and anyons on a trapped-ion processor, *Nature* **626**, 505 (2024).
- [20] S. Xu, Z.-Z. Sun, K. Wang, H. Li, Z. Zhu, H. Dong, J. Deng, X. Zhang, J. Chen, Y. Wu, C. Zhang, F. Jin, X. Zhu, Y. Gao, A. Zhang, N. Wang, Y. Zou, Z. Tan, F. Shen, J. Zhong, Z. Bao, W. Li, W. Jiang, L.-W. Yu, Z. Song, P. Zhang, L. Xiang, Q. Guo, Z. Wang, C. Song, H. Wang, and D.-L. Deng, Non-abelian braiding of Fibonacci anyons with a superconducting processor, *Nature Physics* **20**, 1469 (2024).
- [21] D. J. Thouless, Quantization of particle transport, *Phys. Rev. B* **27**, 6083 (1983).
- [22] K. Wintersperger, C. Braun, F. N. Ünal, A. Eckardt, M. D. Liberto, N. Goldman, I. Bloch, and M. Aidelsburger, Realization of an anomalous Floquet topological system with ultracold atoms, *Nature Physics* **16**, 1058–1063 (2020).
- [23] C. Braun, R. Saint-Jalm, A. Hesse, J. Arceri, I. Bloch, and M. Aidelsburger, Real-space detection and manipulation of topological edge modes with ultracold atoms, *Nature Physics* **20**, 1306 (2024).
- [24] F. Wilczek, Quantum time crystals, *Phys. Rev. Lett.* **109**, 160401 (2012).
- [25] C. W. von Keyserlingk, V. Khemani, and S. L. Sondhi, Absolute stability and spatiotemporal long-range order in Floquet systems, *Phys. Rev. B* **94**, 085112 (2016).
- [26] J. e. a. Zhang, Observation of a discrete time crystal, *Nature* **543**, 217 (2017).
- [27] S. Choi, J. Choi, R. Landig, G. Kucsko, H. Zhou, J. Isoya, F. Jelezko, S. Onoda, H. Sumiya, V. Khemani, C. von Keyserlingk, N. Y. Yao, E. Demler, and M. D. Lukin, Observation of discrete time-crystalline order in a disordered dipolar many-body system, *Nature* **543**, 221–225 (2017).
- [28] S. Pal, N. Nishad, T. S. Mahesh, and G. J. Sreejith, Temporal order in periodically driven spins in star-shaped clusters, *Phys. Rev. Lett.* **120**, 180602 (2018).
- [29] J. Rovny, R. L. Blum, and S. E. Barrett, Observation of discrete-time-crystal signatures in an ordered dipolar many-body system, *Phys. Rev. Lett.* **120**, 180603 (2018).
- [30] X. Mi *et al.*, Time-crystalline eigenstate order on a quantum processor, *Nature* **601**, 531 (2022).
- [31] P. Bruno, Comment on “quantum time crystals”, *Phys. Rev. Lett.* **110**, 118901 (2013).
- [32] P. Nozières, Time crystals: Can diamagnetic currents drive a charge density wave into rotation?, *Europhysics Letters* **103**, 57008 (2013).
- [33] H. Watanabe and M. Oshikawa, Absence of quantum time crystals, *Phys. Rev. Lett.* **114**, 251603 (2015).
- [34] X. Zhang, W. Jiang, J. Deng, K. Wang, J. Chen, P. Zhang, W. Ren, H. Dong, S. Xu, Y. Gao, F. Jin, X. Zhu, Q. Guo, H. Li, C. Song, A. V. Gorshkov, T. Iadecola, F. Liu, Z.-X. Gong, Z. Wang, D.-L. Deng, and H. Wang, Digital quantum simulation of Floquet symmetry-protected topological phases, *Nature* **607**, 468–473 (2022).
- [35] P. T. Dumitrescu, J. G. Bohnet, J. P. Gaebler, A. Hankin, D. Hayes, A. Kumar, B. Neyenhuis, R. Vasseur, and A. C. Potter, Dynamical topological phase realized in a trapped-ion quantum simulator, *Nature* **607**, 463–467 (2022).
- [36] T. B. Wahl, B. Han, and B. Béri, Topologically ordered time crystals, *Nature Communications* **15**, 9845 (2024).
- [37] L. Xiang, W. Jiang, Z. Bao, Z. Song, S. Xu, K. Wang, J. Chen, F. Jin, X. Zhu, Z. Zhu, F. Shen, N. Wang, C. Zhang, Y. Wu, Y. Zou, J. Zhong, Z. Cui, A. Zhang, Z. Tan, T. Li, Y. Gao, J. Deng, X. Zhang, H. Dong, P. Zhang, S. Jiang, W. Li, Z. Lu, Z.-Z. Sun, H. Li, Z. Wang, C. Song, Q. Guo, F. Liu, Z.-X. Gong, A. V. Gorshkov, N. Y. Yao, T. Iadecola, F. Machado, H. Wang,

- and D.-L. Deng, Long-lived topological time-crystalline order on a quantum processor, *Nature Communications* **15**, 8963 (2024).
- [38] I. C. Fulga, M. Maksymenko, M. T. Rieder, N. H. Lindner, and E. Berg, Topology and localization of a periodically driven Kitaev model, *Phys. Rev. B* **99**, 235408 (2019).
- [39] A. Kitaev, Anyons in an exactly solved model and beyond, *Annals of Physics* **321**, 2 (2006), January Special Issue.
- [40] G. Kishony, O. Grossman, N. Lindner, M. Rudner, and E. Berg, *Topological excitations at time vortices in periodically driven systems* (2024), arXiv:2410.17314 [cond-mat.str-el].
- [41] See Supplemental Material.
- [42] H.-K. Jin, J. Knolle, and M. Knap, Fractionalized prethermalization in a driven quantum spin liquid, *Phys. Rev. Lett.* **130**, 226701 (2023).
- [43] W. De Roeck and F. Huveneers, Stability and instability towards delocalization in many-body localization systems, *Phys. Rev. B* **95**, 155129 (2017).
- [44] T. Mori, T. Kuwahara, and K. Saito, Rigorous bound on energy absorption and generic relaxation in periodically driven quantum systems, *Phys. Rev. Lett.* **116**, 120401 (2016).
- [45] D. A. Abanin, W. De Roeck, W. W. Ho, and F. Huveneers, Effective Hamiltonians, prethermalization, and slow energy absorption in periodically driven many-body systems, *Phys. Rev. B* **95**, 014112 (2017).
- [46] S. A. Weidinger and M. Knap, Floquet prethermalization and regimes of heating in a periodically driven, interacting quantum system, *Scientific reports* **7**, 1 (2017).
- [47] D. V. Else, B. Bauer, and C. Nayak, Prethermal phases of matter protected by time-translation symmetry, *Phys. Rev. X* **7**, 011026 (2017).
- [48] A. Chandran, A. Pal, C. R. Laumann, and A. Scardicchio, Many-body localization beyond eigenstates in all dimensions, *Phys. Rev. B* **94**, 144203 (2016).
- [49] K. Fredenhagen and M. Marcu, Charged states in  $\mathbb{Z}_2$  gauge theories, *Communications in Mathematical Physics* **92**, 81 (1983).
- [50] M. Lukin, private communication (2025).
- [51] Google Quantum AI team and collaborators, Suppressing quantum errors by scaling a surface code logical qubit, *Nature* **614**, 676 (2023).
- [52] Google Quantum AI team and collaborators, Quantum error correction below the surface code threshold, *Nature* **10.1038/s41586-024-08449-y** (2024).
- [53] M. Will, T. A. Cochran, E. Rosenberg, B. Jobst, N. M. Eassa, P. Roushan, M. Knap, A. Gammon-Smith, and F. Pollmann, *Probing Non-Equilibrium Topological Order on a Quantum Processor* (2025).
- [54] B. Foxen *et al.* (Google AI Quantum), Demonstrating a continuous set of two-qubit gates for near-term quantum algorithms, *Phys. Rev. Lett.* **125**, 120504 (2020).
- [55] T. White *et al.*, Readout of a quantum processor with high dynamic range Josephson parametric amplifiers, *Applied Physics Letters* **122**, 014001 (2023).
- [56] P. V. Klimov *et al.*, Optimizing quantum gates towards the scale of logical qubits, *Nature Communications* **15**, 2442 (2024).
- [57] A. Bengtsson, A. Opremca, M. Khezri, D. Sank, A. Bourassa, K. J. Satzinger, S. Hong, C. Erickson, B. J. Lester, K. C. Miao, A. N. Korotkov, J. Kelly, Z. Chen, and P. V. Klimov, Model-based optimization of superconducting qubit readout, *Phys. Rev. Lett.* **132**, 100603 (2024).
- [58] J. Kelly, P. O'Malley, M. Neeley, H. Neven, and J. M. Martinis, *Physical qubit calibration on a directed acyclic graph* (2018), arXiv:1803.03226 [quant-ph].
- [59] Google Quantum AI team and collaborators, Quantum supremacy using a programmable superconducting processor, *Nature* **574**, 505 (2019).
- [60] J. Bylander, S. Gustavsson, F. Yan, F. Yoshihara, K. Harrabi, G. Fitch, D. G. Cory, Y. Nakamura, J.-S. Tsai, and W. D. Oliver, Noise spectroscopy through dynamical decoupling with a superconducting flux qubit, *Nature Physics* **7**, 565–570 (2011).
- [61] J. J. Wallman and J. Emerson, Noise tailoring for scalable quantum computation via randomized compiling, *Phys. Rev. A* **94**, 052325 (2016).
- [62] A. Hashim, R. K. Naik, A. Morvan, J.-L. Ville, B. Mitchell, J. M. Kreikebaum, M. Davis, E. Smith, C. Iancu, K. P. O'Brien, I. Hincks, J. J. Wallman, J. Emerson, and I. Siddiqi, Randomized compiling for scalable quantum computing on a noisy superconducting quantum processor, *Phys. Rev. X* **11**, 041039 (2021).
- [63] J. Hauschild and F. Pollmann, Efficient numerical simulations with Tensor Networks: Tensor Network Python (TeNPy), *SciPost Phys. Lect. Notes* , 5 (2018).
- [64] U. Schollwöck, The density-matrix renormalization group in the age of matrix product states, *Annals of Physics* **326**, 96 (2011), January 2011 Special Issue.
- [65] G. Vidal, Efficient simulation of one-dimensional quantum many-body systems, *Phys. Rev. Lett.* **93**, 040502 (2004).
- [66] The entanglement entropy for the state without an  $e$  anyon is the same, so we only show the data for the initial state with an  $e$  anyon.



# Supplementary Information for: Probing Non-Equilibrium Topological Order on a Quantum Processor

## FLOQUET KITAEV MODEL

The Floquet Kitaev model is well understood due to a Majorana representation of the spins, which reveals the free-fermion solvability of the model [6, 38]. On each site, four Majorana operators  $\{c, b^x, b^y, b^z\}$  can be defined, such that the Pauli operations on the spin sites are

$$X_j = ic_j b_j^x, \quad Y_j = ic_j b_j^y, \quad Z_j = ic_j b_j^z, \quad (9)$$

where  $c_j^2 = 1$  and  $\{c_j, c_k\} = 0$  for  $j \neq k$ , and similarly for  $b_j^\alpha$ , see Fig. 5a. This representation enlarges the Hilbert space, and the physical Hilbert space corresponds to the set of states  $|\psi\rangle$  such that  $c_j b_j^x b_j^y b_j^z |\psi\rangle = |\psi\rangle$  for all  $j$ . The model has a set of conserved quantities  $u_{jk} = ib_j^{\alpha_{jk}} b_k^{\alpha_{jk}}$ , where  $\alpha_{jk}$  is the Pauli operator associated with that bond. Note that these are conserved not just stroboscopically, but at all points throughout the drive. These can be thought of as a  $\mathbb{Z}_2$  gauge field, and products of these operators around closed loops correspond to physical gauge-invariant conserved quantities, the fundamental instances of which are the flux operators

$$W_P = \prod_{\langle i,j \rangle \in P} u_{ij} \quad (10)$$

illustrated in Fig. 5a. These measure the flux through each of the plaquettes, and we refer to  $W_P = +1$  as flux-free. Each of the driving terms is then of the form

$$\exp \left\{ -JT \frac{\pi}{4} \sum_{\langle ij \rangle} u_{ij} c_i c_j \right\}, \quad (11)$$

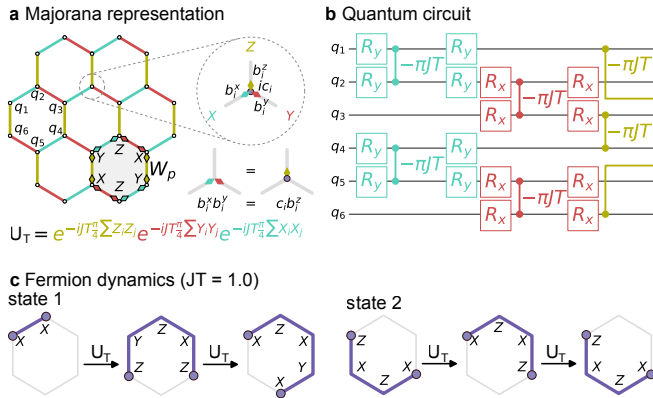


FIG. 5. **a** Majorana representation. **b** Quantum circuit for one plaquette for one Floquet cycle in terms of single qubit rotations and C-PHASE gates. **c** Two examples of fermion dynamics at the fine-tuned point of  $JT = 1$ . State 2 is invariant under two driving cycles.

which is quadratic in the  $c_i$  Majorana fermion operators. These correspond to hopping operators for the  $c$ -fermions, and perform a Majorana swap when  $JT = 1$  (M-SWAP). This driving can be efficiently implemented on a quantum processor using C-PHASE gates and single qubit rotations, as shown for the example of a single hexagonal plaquette in Fig. 5b.

To monitor the dynamics of the emergent Majorana modes, we define measurable operators by pairing them into complex fermions. The paired fermion operators are then defined as  $f_{jk} = (c_j + i\phi_{jk}c_k)/2$ , where

$$\phi_{jk} = \prod_{\langle l,m \rangle \in \text{path}(j,k)} u_{lm} \quad (12)$$

is a gauge string consisting of a product of the gauge fields along a path connecting the paired sites. This leads to a density operator

$$n_F(j, k) = \frac{1}{2} (i\phi_{jk}c_jc_k + 1), \quad (13)$$

which can be written as a Pauli string. Under the Floquet dynamics these paired fermions move around the system, as illustrated in Fig. 5c.

## EXPERIMENTAL PROCEDURES

CZ and CPHASE gates are implemented by setting the qubit detuning close to the anharmonicity and harnessing a diabatic  $|11\rangle \rightleftharpoons |20\rangle$  swap to generate an arbitrary CPHASE angle with minimal leakage [54]. Dominant errors come from CZ/CPHASE entangling gates and final readout [55], see Fig. 6. The Snake optimizer [56, 57] has been used to optimize qubits, coupler, and readout parameters. A smaller contribution to the total error comes from the single-qubit microwave gates, which are calibrated using Google's Optimus calibration tools [58, 59].

### Dynamical Decoupling

Idle qubits are exposed to errors over time. In particular, this is critical for Hadamard tests such as the Floquet braiding experiment. In contrast to all other qubits, the ancilla is not part of the Floquet time evolution and is idle during this time. To quantify those errors under experimental conditions, we use the same circuit as in the actual Floquet braiding experiment but do not couple the ancilla to the system, see Fig. 7a. Therefore, the

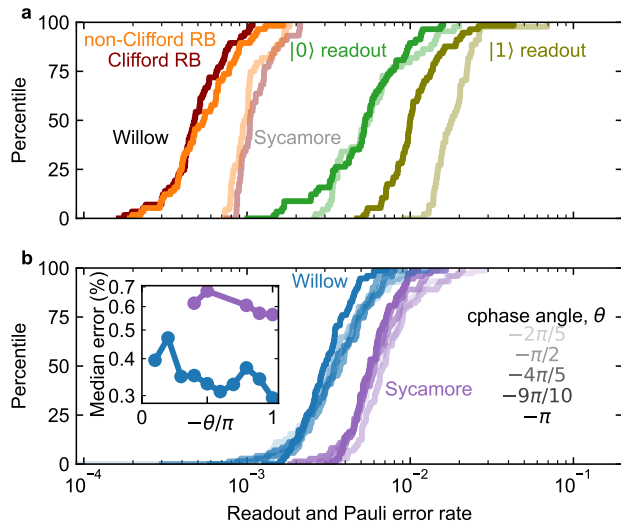


FIG. 6. **Experimental fidelities.** **a** Representative cumulative distribution functions of relevant gate and measurement errors. Single qubit Clifford and non-Clifford Pauli errors, determined from randomized benchmarking (RB), are shown in red and orange with median errors of 0.10% and 0.096%, respectively, on the Sycamore device and 0.047% and 0.054% on the Willow device.  $|0\rangle$  state and  $|1\rangle$  state readout errors, determined from sampling random bitstrings, are shown in green and olive with median errors of 0.55% and 1.8%, respectively on the Sycamore device and 0.53% and 1.0% on the Willow device. **b** Inferred CZ Pauli errors ( $\theta = -\pi$ ), determined from cross-entropy benchmarking, are shown in purple (Sycamore) and blue (Willow) with a median error of 0.56% on the Sycamore device and 0.29% on the Willow device. Distribution functions for inferred errors of CPHASE gates with selected angles used in this work are also shown ( $\theta \in \{-9\pi/10, -4\pi/5, -\pi/2, -2\pi/5\}$ ). Lighter shades correspond to angles closer to zero. The inset shows the median error rates for all cphase angles used in this work. To implement non-Clifford RB, we replace the standard depth- $n$  RB sequence, which consists of  $n-1$  random Clifford gates and a final Clifford gate that inverts the sequence, with  $U_f X U_{\frac{n-1}{2}} \dots X U_0$ , where each  $U_i$  is a Haar random single-qubit unitary, and  $U_f$  is computed to invert the whole sequence. The error rate thus obtained, which includes approximately equal contributions from the Clifford  $X$  gates and the non-Clifford  $U_i$  gates, is what is plotted in panel **a** as “1Q non-Clifford.”

ancilla should remain in the  $|+\rangle$  state as no other operation is performed on it. In the Hadamard test, we would measure the expectation value of  $\langle X_A \rangle$  and  $\langle Y_A \rangle$  and we therefore probe those two expectation values here. In Fig. 7b, we would expect to measure  $+1$  at all times for  $\langle X_A \rangle$  and  $0$  for  $\langle Y_A \rangle$ . However, we observe that  $\langle X_A \rangle$  decreases quickly, while  $\langle Y_A \rangle$  increases at the same time. To mitigate this effect, we apply a simple form of dynamical decoupling [60] by randomly applying  $X$ - $X$  or  $Y$ - $Y$  sequences on the idle ancilla. Figure 7c shows that this technique effectively reduces these errors.

## Randomized Compiling

To address CZ-gate dependent errors, which can arise from imperfect gate calibration, we have applied randomized compiling to all CZ gates in all experiments. This technique [61, 62], involves inserting sets of Pauli operators before and after the CZ gates, leaving the total circuit invariant while significantly enhancing the overall performance.

## EXTENDED DATA AND DERIVATIONS

### Preparation of initial states

In order to prepare a flux-free state, we use the circuit shown in Fig. 8 for the 7 plaquette set-up and the circuit shown in Fig. 10 for the large system, which was introduced in [16, 42]. After this initial preparation, fermions are paired vertically on  $z$ -bonds. In the main text we denote this flux-free state as  $|\Psi_{\text{FF}}\rangle$ . For all experiments, we first prepare this flux-free state and then rearrange the fermions depending on the initial state needed. In order to preserve the fluxes, fermions can be rearranged by applying  $e^{-iJT \frac{\pi}{4} (\alpha_{jk})_j (\alpha_{jk})_k}$  with  $JT = 1$  so that those operators correspond to swap operations of  $c$ -Majoranas of the respective bond (M-SWAP). Choosing the operator depending on the type of bond ( $x$ ,  $y$  or  $z$ ) preserves the flux. Fig. 9 illustrates the step-by-step rearrangement of fermions for the initial state of Fig. 1b. In the flux-free state, all fermions are paired vertically along the  $z$ -bonds. Applying M-SWAP gates with  $JT = 1$  (as depicted), these pairs are rearranged perfectly, resulting in one bulk fermion that remains invariant under a period of  $N = 2$  and edge fermions.

The circuit for the flux-free state preparation of the 58 qubit set-up used in the  $e$ - $m$  transmutation experiment as well as the two layers of M-SWAP gates used for rearrangement of fermions is shown in Fig. 10. For all other experiments, state preparation is detailed in the figures in the main text. Generally, we have chosen initial states to ensure that the circuits are as shallow as possible while at the same time yielding the clearest experimental results. For example, in the case of the spectral function, the only requirement for the initial state, apart from being flux-free, is that the protruding bond hosts a perfectly occupied fermion. Beyond that, the specific pairing of Majoranas in the rest of the system is irrelevant. As such, starting directly from the flux-free state yields the shallowest circuit. Notably, we have this freedom in the initial state, as we are probing properties of the Floquet operator rather than fine-tuned initial states.

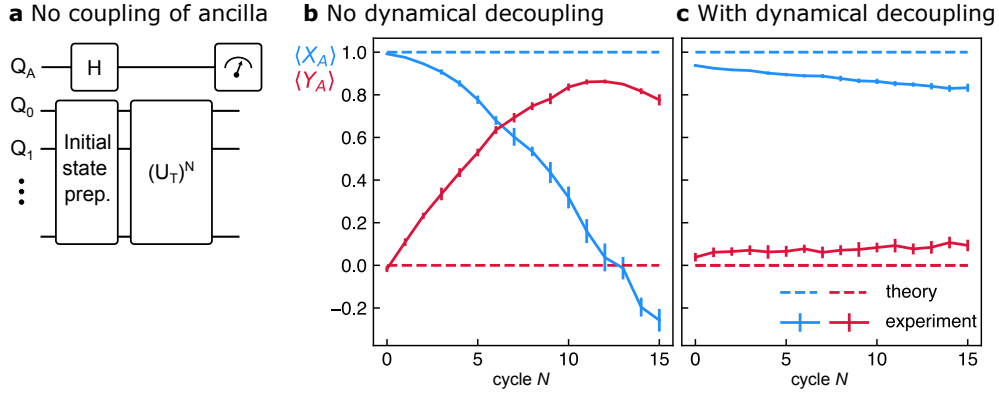


FIG. 7. **Dynamical Decoupling.** **a** Circuit to test stability of ancilla. To mimic the Floquet braiding experiment, we use the same circuit except for not coupling the ancilla to the system. **b** Without dynamical decoupling the ancilla is idle during time evolution and drifts away from being in the  $|+\rangle$  state. **c** Adding dynamical decoupling by randomly applying  $X$ - $X$  and  $Y$ - $Y$  pairs to the ancilla resolves those errors.

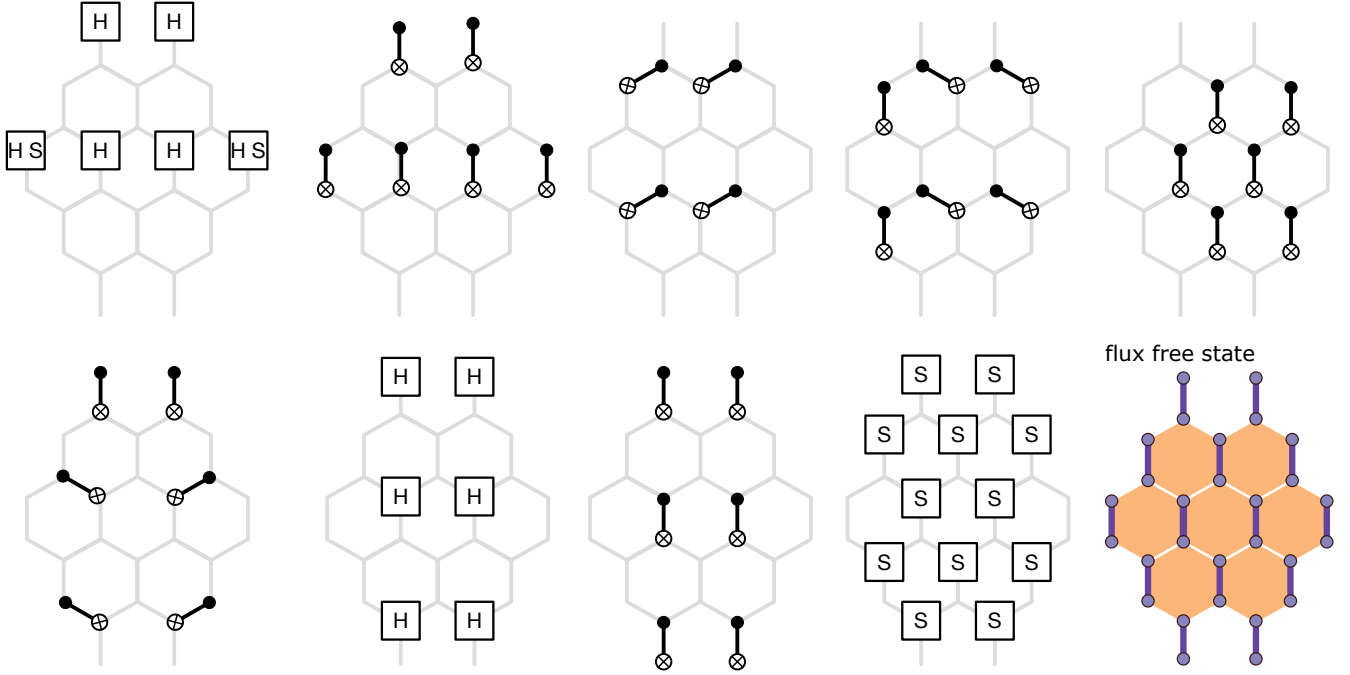


FIG. 8. **Flux-free state preparation in two-site gates.** We have adopted the preparation scheme of [16, 42] for the preparation of a flux-free state. In the flux-free state  $|\Psi_{\text{FF}}\rangle$  all fermions are paired vertically on  $z$ -bonds, as shown in purple and all fluxes have expectation value of one.

### Floquet Braiding

In Fig. 2, we present post-selected data of the Floquet braiding experiment. The Floquet drive without disorder conserves the fluxes in the system, allowing us to use those operators for post selection. Since all flux operators commute with each other, they can in theory be measured simultaneously. However, this requires a deep two-site gate circuit in general. Therefore, it is important

to balance between adding extra layers and post selecting on as many plaquettes as possible.

For two plaquettes, Figs. 11a–c illustrate how a single additional layer of CZ gates allows us to simultaneously measure the fluxes of two adjacent plaquettes. In Fig. 11a we show two plaquettes sharing a  $y$ -bond. To extract these two fluxes, we have to measure the expectation values of  $XZ$  and  $ZX$  simultaneously. This is achievable by applying a CZ gate on this bond, see Fig. 11b,

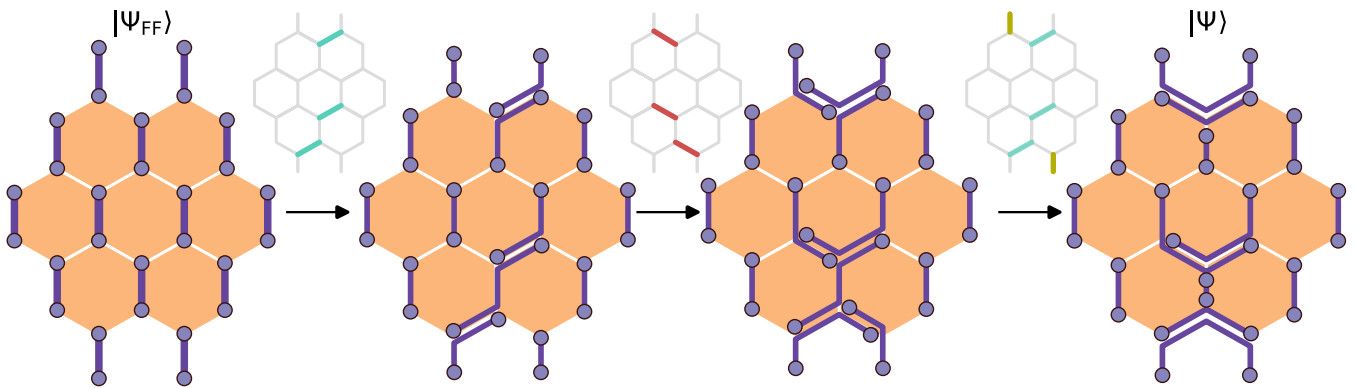


FIG. 9. **Initial state preparation of Fig. 1b.** Starting from the flux-free state, M-SWAP gates are used to prepare the initial state of Fig. 1b.

which rotates those two sites into the eigenbasis of the two operators. By measuring the operators depicted in Fig. 11c, we can measure the two fluxes at the same time. To simultaneously extract the six flux operators shaded in blue in Fig. 11d, we apply this circuit on all shared bonds. Depending on the bond, additional rotations are required to align with the eigenbasis of  $XY$  and  $YX$  ( $z$ -bond) or  $ZY$  and  $YZ$  ( $x$ -bond).

In Fig. 11e, we present both post-selected and non-post-selected data, demonstrating that post selection significantly improves the radial component. Radial and angular error bars have been calculated from real and imaginary standard deviation by the following equations:

$$\sigma_r = \frac{1}{r} \sqrt{(\Re \times \sigma_{\Re})^2 + (\Im \times \sigma_{\Im})^2} \quad (14)$$

$$\sigma_{\Phi} = \frac{1}{r^2} \sqrt{(\Im \times \sigma_{\Re})^2 + (\Re \times \sigma_{\Im})^2} \quad (15)$$

with  $\Re$  ( $\Im$ ) being the mean value of the real (imaginary part) at a given time step.

### Spectral Function

The Floquet Kitaev model in the FTO phase hosts a chiral edge mode of Majorana fermions. To investigate the stability of these edge modes, we measure a Majorana spectral function along the edge of the system. Experimentally, this measurement is achievable by evaluating Pauli strings along the edge.

The key idea is to add an extra site to the system, which is not subject to the time evolution. By initializing a fermion on this protruding bond, only the end of the fermion within the driven part of the system will move along the edge, while the other end remains stationary outside the system. This setup allows us to compute the expectation value:

$$\langle \Psi_0 | P_j(N) P_0(0) | \Psi_0 \rangle. \quad (16)$$

This expectation value relates to a Majorana spectral function of the form:

$$\langle \Psi_0 | c_j(N) c_0(0) | \Psi_0 \rangle. \quad (17)$$

First, we note that the two Pauli strings overlap on the protruding bond. By rewriting these Pauli strings in terms of Majorana fermions, as illustrated in Fig. 14b, we observe that the non-time-evolved parts cancel out to one. This results in a Majorana-Majorana spectral function, allowing us to probe the stability of the chiral edge modes.

In Fig. 12 we present exact diagonalization data for the spectral function. In contrast to the experimental data presented in the main text Fig. 3d the signal does not decay for  $JT = 1$ . We attribute the decay in the experiment to a combination of coherent errors and decoherence in the device. Still, the feature of a chiral Majorana edge mode is well observed experimentally. In Fig. 13 we present experimental data without post selection. In contrast, Fig. 3d in the main text we present post selected data, where we have used the central plaquette of the set up for post selection. Note, that it is not possible to post select on more plaquettes without a large overhead of two-site gates. The standard deviation of the data presented in the main text is shown in Fig. 15. For the experimental data with a disordered field, we present the standard deviation over 20 different disorder configurations. We have applied a cosine window function of power to the 6<sup>th</sup> to the data before Fourier transforming in time. At the fine-tuned point of  $JT = 1$   $c$ -Majoranas are perfectly transferred to a neighboring site.  $P_0$  is perfectly transferred into  $P_j(4)$  after four time steps. We would thus expect the correlation in Eq. 16 to be one. We define the Fourier transform in terms of the translation matrix and its eigenvectors  $\hat{F}|v_q\rangle = e^{iq}|v_q\rangle$  at  $JT = 1$ . The Fourier transform of a state  $|\Psi\rangle$  is then given by the overlap:

$$|\Psi_q\rangle = \langle v_q | \Psi \rangle \quad (18)$$

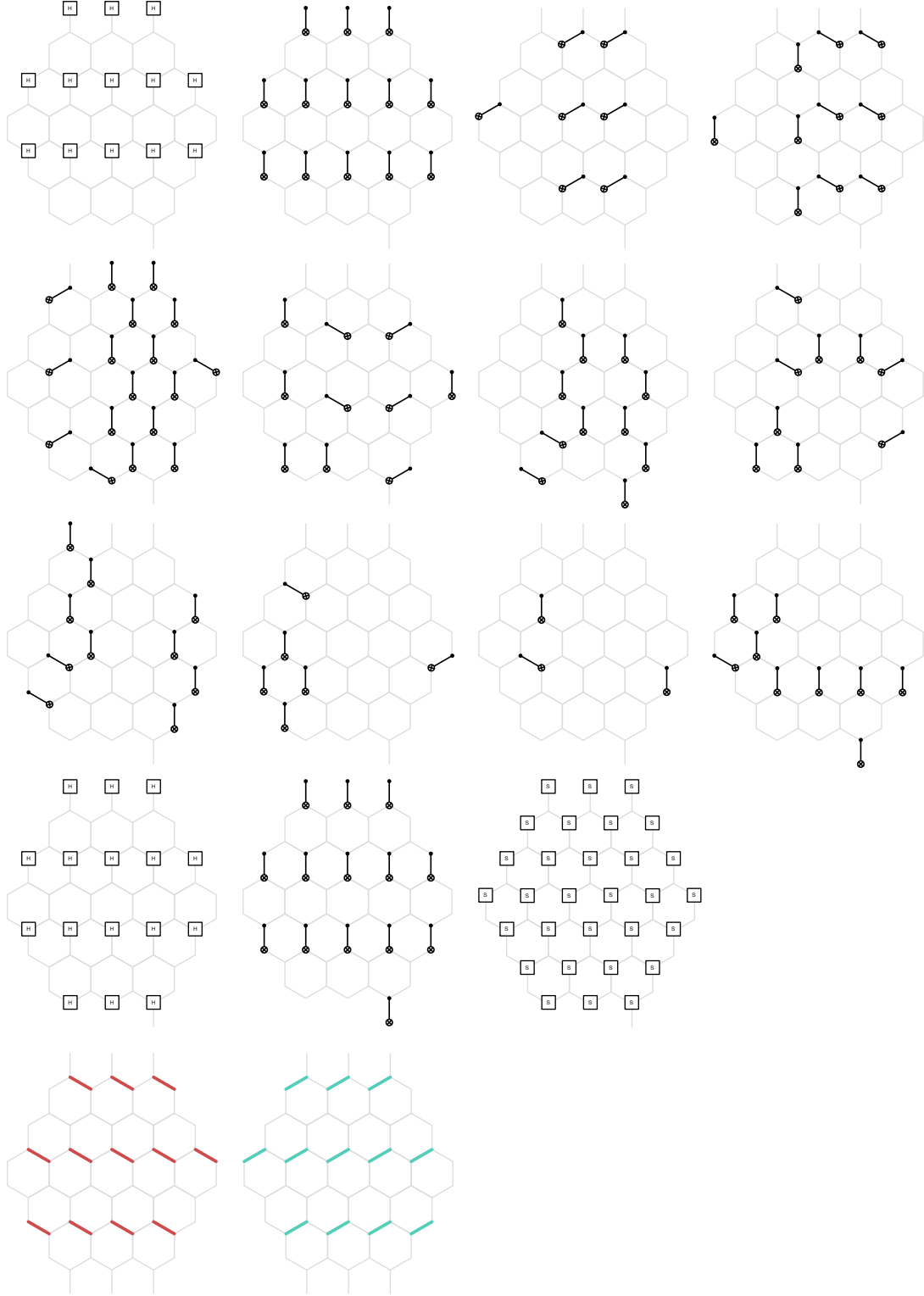


FIG. 10. **Initial state preparation for  $e$ - $m$  transmutation for Fig. 4.** After preparing the flux-free state, applying M-SWAP gates on  $y$ - and then  $x$ -bonds prepares the initial state for the  $e$ - $m$  transmutation experiment.

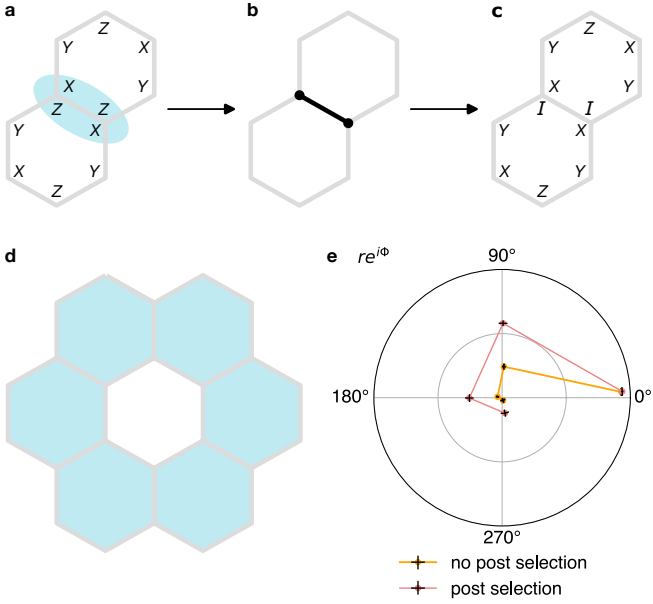


FIG. 11. **Post selection for  $e$ - $m$  transmutation.** **a-c** To measure two flux operators at the same time, one has to rotate the shared bond into an eigenbasis of the operators. **a** Shows exemplary two plaquettes and the Pauli strings defining the flux operators on those plaquettes. In blue the shared bond is highlighted. **b** Applying a CZ gate on the shared bond rotates the bond into a basis, such that both flux operators can be measured simultaneously. **c** In the new basis we have to measure the shown operators to evaluate the flux. **d** Using this scheme on shared bonds, we can perform post selection on shaded 6 plaquettes at the same time with only one extra CZ layer. **e** Comparison of (non)-post selected experimental data.  $N_{\text{shots}} = 5 \times 10^5$ ,  $N_{\text{twirling}} = 20$ .

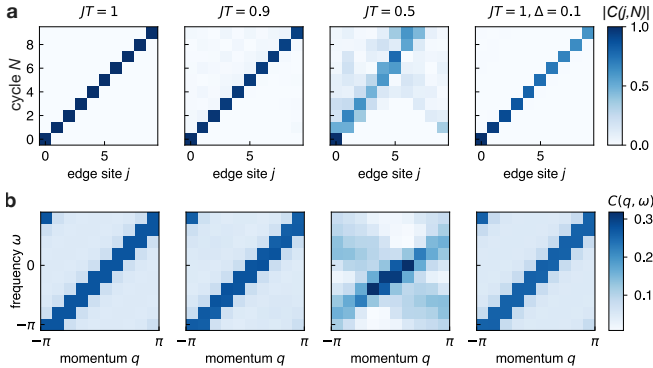


FIG. 12. **Exact diagonalization results.** Shown is exact diagonalization data, for the experiment shown in Fig. 3. **a** Measured signal. **b** Fourier transformed data.

where  $N$  is the number of edge sites.

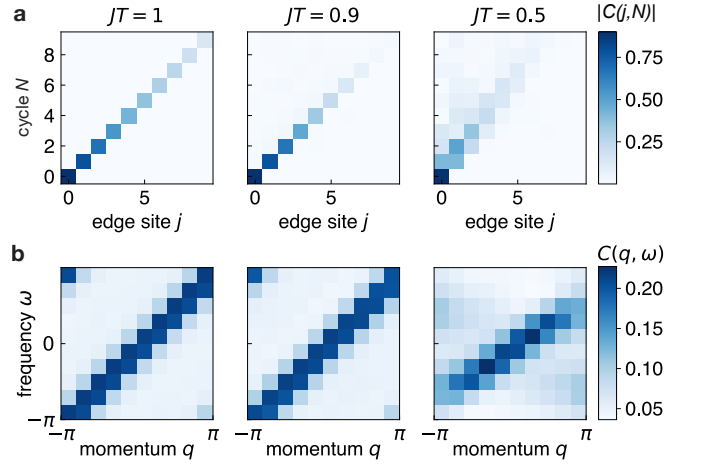


FIG. 13. **Spectral function without post selection on central plaquette.** For the Floquet time evolution without an additional field, the fluxes are conserved and can be used for post selection. In Fig. 3e we present data with post selection on the central plaquette of the system. Even without post selection the signal is well visible. **a** Measured signal. **b** Fourier transformed data.

### $e$ - $m$ transmutation

In the bulk, the FTO phase is characterized by  $\mathbb{Z}_2$  topological order, hosting  $e$ ,  $m$  and  $\psi$  anyons [6]. This property can directly be observed at  $JT = 1$  for fermions paired along the diagonal of a plaquette, depicted as state 2 in Fig. 5c. In this case, such a bulk fermion evolves back to its original position after driving twice. In the following we will use the convention that a bulk fermion is occupied if the Pauli string, which measures the occupation  $n_F$ , defined as in state 2, is equal to  $+1$ . The fermion parity  $P_F = (-1)^{n_F} = \pm 1$  picks up the flux of the respective plaquette under driving

$$U_T^\dagger P_F U_T = W_P P_F. \quad (19)$$

If the flux through a plaquette is  $+1$ , the fermion occupation in that plaquette remains constant during time evolution. However, if the flux is  $W_P = -1$ , the fermion occupation will alternate after each driving cycle, resulting in a periodicity of  $N = 2$ . In general a  $\psi$  anyon corresponds to an occupied bulk fermion  $n_F = 1$  and a pair of them can be created on top of the flux-free state by applying a Pauli string as exemplary shown in Fig. 16a. Conversely, creating a flux defect  $W_P = -1$  without changing the fermion occupation  $n_F = 0$  corresponds to an  $m$  anyon. An example of the creation of two  $m$  anyons is shown in Fig. 16b. The combination of a flipped flux  $W_P = -1$  and an occupied fermion  $n_F = 1$  leads to an  $e$  anyon, see e.g. Fig. 16c. In the FTO phase, an  $e$  anyon in the bulk will evolve into an  $m$  anyon and after  $N = 2$  cycles back into an  $e$  anyon. To measure this  $\mathbb{Z}_2$  topological order, one can measure an  $e$  loop around

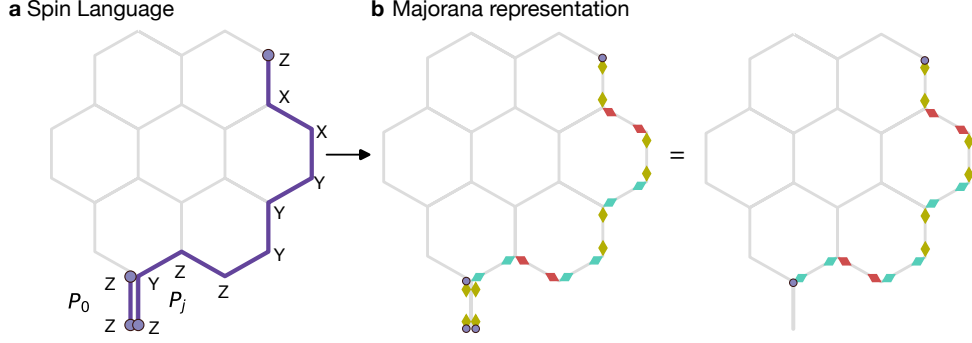


FIG. 14. **Derivation of the spectral function.** **a** Example of Pauli strings, which have to be evaluated in order to calculate the spectral function. The purple Pauli string originates out of the black fermion after time evolution of  $N = 4$ . **b** Pauli strings can be rewritten in terms of Majoranas. For the specific example, the decomposition is illustrated. The two fermions overlap on the protruding bond. There, the Majorana operators occur twice and thus multiply to one. Thus one is left with the string of Majoranas shown on the right hand side.

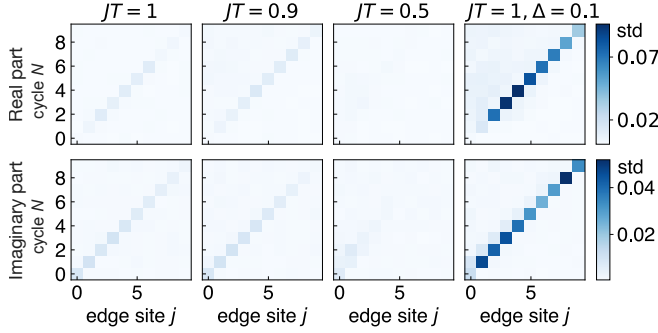


FIG. 15. **Standard deviations for real and imaginary part of the real space spectral function of Fig. 3d.** For the disordered Floquet case we show the standard deviation calculated over the 20 different disorder realizations. For each of those data sets, the standard deviation is of the magnitude of the clean Floquet cases.

the center anyon. This  $e$  loop is an  $e$  anyon dragged around e.g. a plaquette and then annihilated in the end. This operator commutes with an  $e$  anyon, thus giving  $+1$ , but anticommutes with the  $m$  anyon thus giving  $-1$ .

In the main text we present results of the bulk invariant, see Fig. 4c, which shows clear oscillations in the FTO phase that are absent in the non-abelian Kitaev phase.

In Fig. 17 we present time evolution of the  $e$  loop operator for the excited and non-excited state separately. Since expectation values approach zero and we are sampling a finite number of measurements, we add a small shift of 0.01 to the denominator of the order parameter  $\eta(N)$ . The mean is calculated by

$$\eta(N) = \frac{1}{N_{\text{twirling}}} \sum_{i \in N_{\text{twirling}}} \frac{\langle \Psi_e | O(N) | \Psi_e \rangle_i}{|\langle \Psi_0 | O(N) | \Psi_0 \rangle_i| + 0.01}, \quad (20)$$

where we average over ratios of loop expectation values

with and without anyons of same twirling sets. The standard deviation is also extracted from those sets. Fig. 18 shows the order parameter  $\eta(N)$  for different combinations of  $JT$  and  $\Delta$ . Applying a cosine window function of power 4<sup>th</sup> and Fourier transforming those datasets yields the spectra shown in Fig. 19. In the FTO phase we expect a peak at  $\pi$ , whereas in the Kitaev phase at zero. Thus the difference of  $|\eta(\omega = \pi)| - |\eta(\omega = 0)|$  has different signs in the two phases. This difference is shown in the main text in Fig. 4d. In Fig. 20 we give standard deviations in addition to the mean values at zero and  $\pi$  momentum.

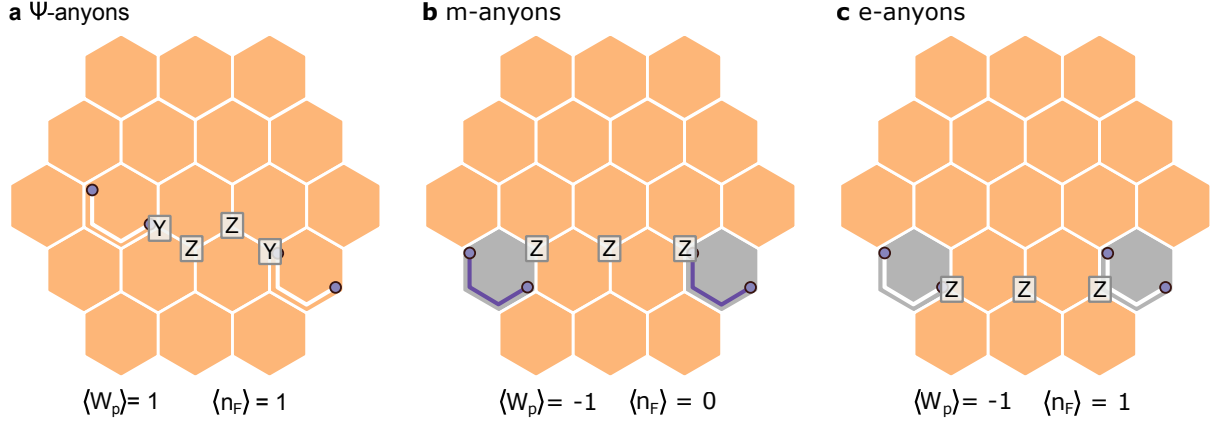


FIG. 16. **Anyonic excitations.** **a** Applying the shown Pauli string leads to the change of occupation of shown bulk fermions resulting in two  $\psi$  anyons. **b** Flipping two fluxes (shown in grey) creates two  $m$  anyons. **c** The combination of flipped flux and fermion occupation within a plaquette defines an  $e$  anyon. The shown Pauli string creates two  $e$  anyons separated by two plaquettes.

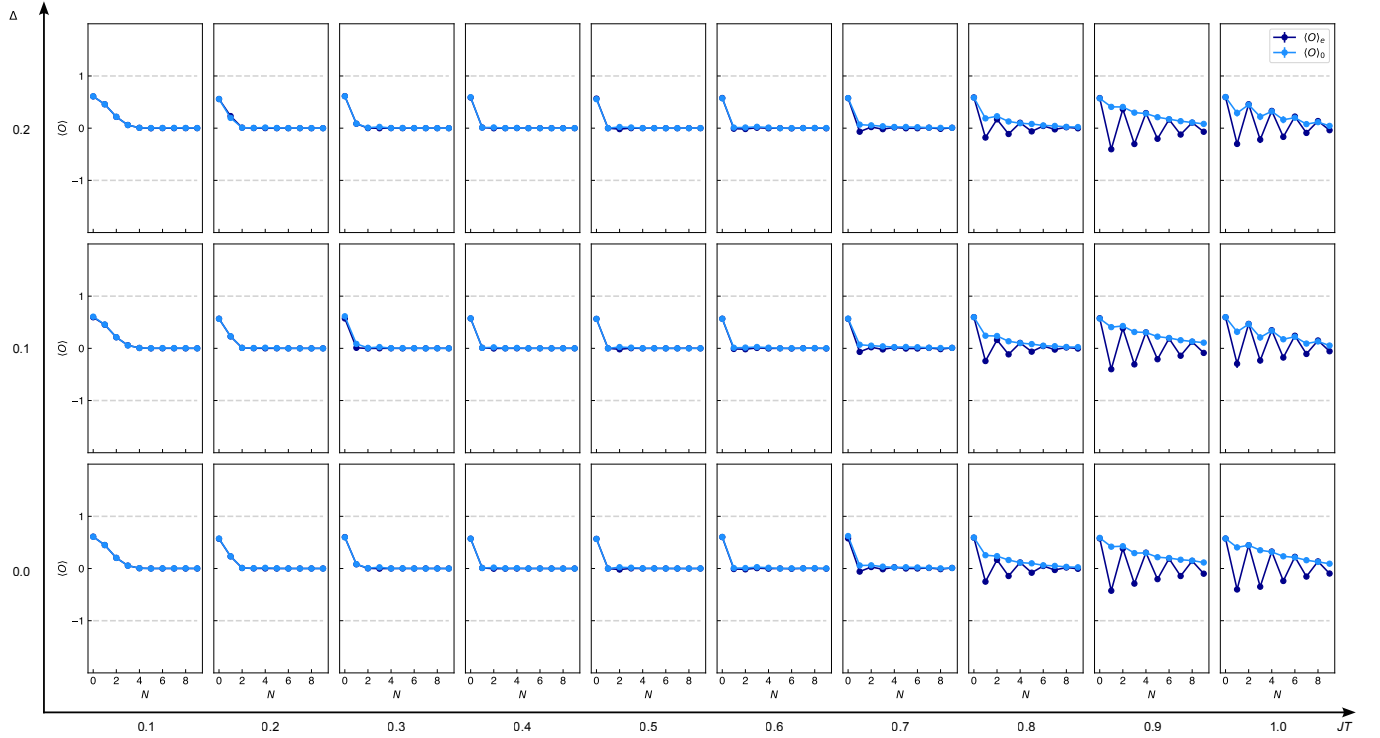


FIG. 17. **Expectation value of loop operators.** In order to extract the phase diagram in Fig. 4e we measure the loop operator over time for an initial state with  $\langle \langle O \rangle_e \rangle$  and without  $\langle \langle O \rangle_0 \rangle$  an  $e$  anyon pair. The  $e$  anyons are transmuted into  $m$  anyons by applying one Floquet cycle in the FTO phase. This is reflected by the loop operator alternating its sign.



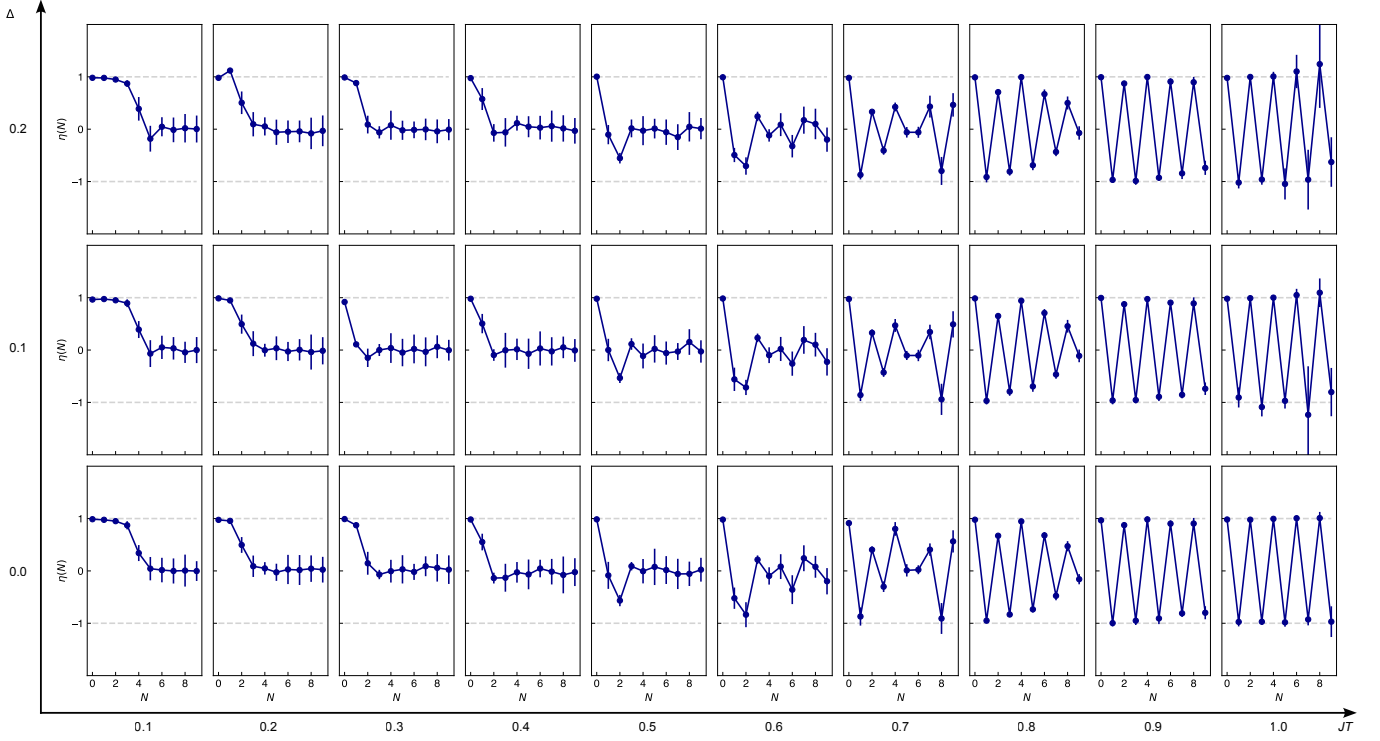


FIG. 18. **Order parameter.** In the spirit of the Fredenhagen-Marcu operator we define the order parameter as the ratio of the expectation value of the loop operator of the initial state with the  $e$  anyons divided by the loop operator without the pair. Since both expectation values decay to zero, see Fig. 17, we add 0.01 to the denominator. In the FTO phase the order parameter shows clear oscillations, which are absent in the Kitaev phase.

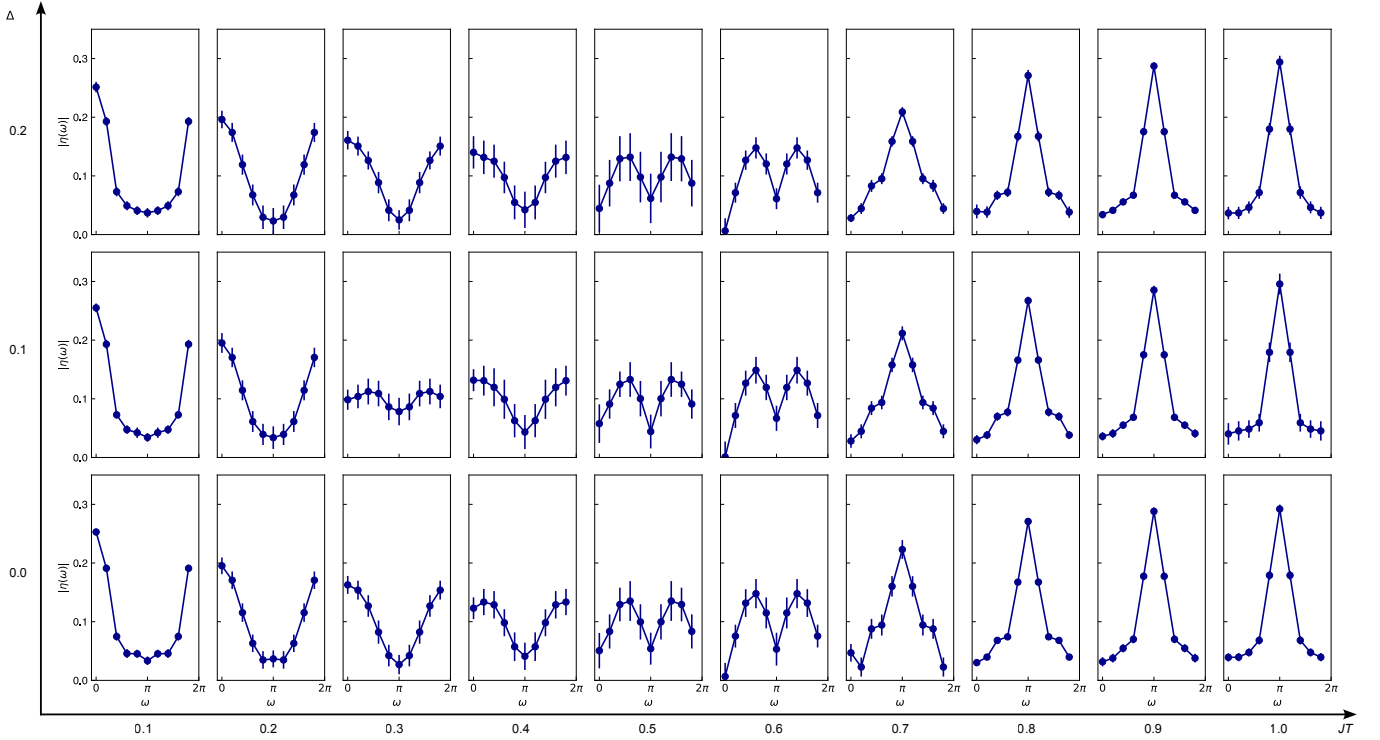


FIG. 19. **Fourier transform of the order parameter for all combinations of  $JT$  and  $\Delta$ .** Fourier transforming the order parameter shown in Fig. 18 reveals a peak at  $\pi$  in the FTO phase and a peak at zero in the Kitaev phase. Using the difference of those two values we extracted the phase diagram shown in the main text Fig. 4e.



FIG. 20. Phase diagram in Fig. 4e including standard deviations at  $\pi$  and zero. Subtracting the value of the Fourier transform of the order parameter at momentum  $\pi$  and zero reveals the phase diagram of the two phases.

## MATRIX-PRODUCT STATE SIMULATIONS

In the following, we simulate the  $e$ - $m$  transmutation using matrix-product states (MPS) to get an estimate for the computational hardness of simulating the experiments presented in the main text. We use the Python library TeNPy for our simulations [63].

For our simulations, we consider the experiment in Fig. 4 in the main text. To order the sites into a one-dimensional geometry suitable for MPS simulations, we start from the site at the bottom of the bottom-left hexagon and move up diagonally along  $y$ - and  $z$ -bonds until we reach the boundary of the system, before moving to the next diagonal and starting at the bottom. This way, sites sharing a  $y$ - or  $z$ -bond remain neighbors in the 1D geometry, and only  $x$ -bonds become long-range. The initial state  $|\psi_0\rangle$  (Fig. 4b, middle) is a stabilizer state, so we use DMRG [63, 64] to obtain the simultaneous eigenstate of all its stabilizer Pauli strings without having to run the full state preparation circuit. The  $e$  anyon can be created, as in the experiment, by applying onsite  $Z$ -gates to the MPS tensors. The gates on the  $x$ -bonds can be written as a matrix-product operator (MPO) with bond dimension two acting between the two (non-neighboring) sites. Applying the MPO to the MPS doubles the bond dimension, after which we truncate back to the maximal bond dimension using SVDs. Since all sites sharing a  $y$ - or  $z$ -bond are neighbors, we can apply these gates as in TEBD [65], sweeping left to right when applying the gates on the  $y$ -bonds and sweeping back right to left when applying the gates on the  $z$ -bonds. If we include the disordered  $Z$ -field, the fourth time step consists only of single-qubit rotations that can be directly applied to the corresponding MPS tensor.

First, we consider the fine-tuned point with  $JT = 1.0$  and without disorder (i.e.  $\Delta = 0.0$ ). Fig. 21a shows the maximal entanglement entropy of all bonds at each time step, for the initial state with an  $e$  anyon. [66] Different marker shapes and shades of red denote the different bond dimensions used for the simulation. The entanglement entropy saturates at  $S = 9 \log(2)$ , indicating that at least a bond dimension of  $\chi = 512$  is needed. The simulation data with  $\chi = 512$  and  $\chi = 1024$  do not overlap because intermediate steps in the Floquet cycle can further increase the bond dimension, which then gets truncated in the simulation with  $\chi = 512$ . Since the initial state is a stabilizer state, we can calculate the entanglement entropy (and the required bond dimension) for larger system sizes. The inset shows the entanglement entropy of the initial state against the total number of qubits when cutting the system from the top left plaquette to the bottom right plaquette for an increasing number of rings. Asymptotically, the entanglement entropy scales as  $S(N_Q) \sim \sqrt{2/3} N_Q \log(2)$  (dashed line), where  $N_Q$  is the total number of qubits in the sys-

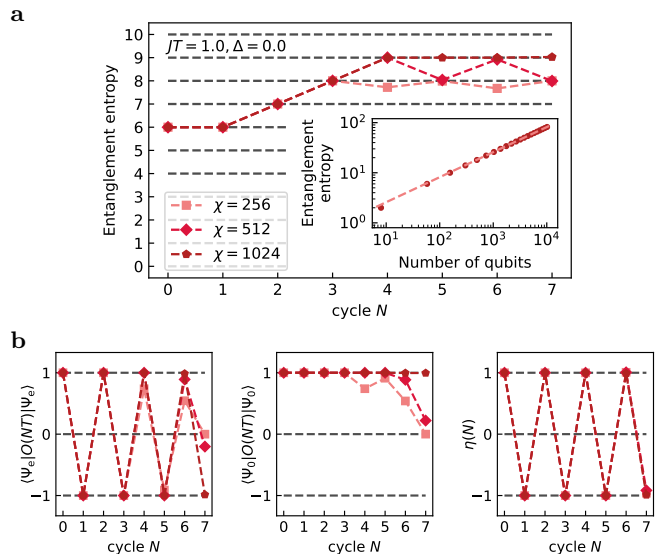


FIG. 21. **MPS simulation of the  $e$ - $m$  transmutation at the fine-tuned point with  $JT = 1.0$  and  $\Delta = 0.0$ .** **a** The maximal entanglement entropy of all bonds at each time step in units of  $\log(2)$ . For visual clarity we only show the entanglement entropy for the simulation of the initial state with an  $e$  anyon, the results for the initial state without an  $e$  anyon are the same. Inset: The red dots show the entanglement entropy of the initial state when increasing the number of rings in the system, the simulated system corresponds to three rings or 58 qubits. The light red dashed line shows the asymptotic scaling  $S(N_Q) \sim \sqrt{2/3} N_Q \log(2)$ , where  $N_Q$  is the total number of qubits in the system. **b** Left to right: The expectation value of the loop operator starting from a state with an  $e$  anyon, without an  $e$  anyon, and their ratio which gives the order parameter defined in Eq. (8).

tem. This translates to a required bond dimension of  $\chi \sim 2\sqrt{2/3} N_Q$ , which scales superpolynomially with the number of qubits. Fig. 21b shows, from left to right, the expectation value of the loop operator when starting from the state with an  $e$  anyon, when starting from the state without an  $e$  anyon, and the order parameter  $\eta(N)$  defined in Eq. (8), which is the ratio of the two expectation values. Using a bond dimension  $\chi = 1024$ , we see that the expectation value of the loop operator persistently oscillates between  $+1$  and  $-1$  if we start from the state with an  $e$  anyon, and remains perfectly at  $+1$  if we start without an  $e$  anyon. Any smaller bond dimension leads to a decay of the expectation values, which, remarkably though, cancels when taking their ratio such that the order parameter behaves correctly for all bond dimensions.

Next, we consider the case where  $JT = 1.0$  and we include the disordered field with strength  $\Delta = 0.2$ . Note that compared to the previous fine-tuned example with  $JT = 1.0$  and  $\Delta = 0.0$ , the time evolution now neither corresponds to a Clifford circuit, which could be efficiently simulated using stabilizer methods, nor does

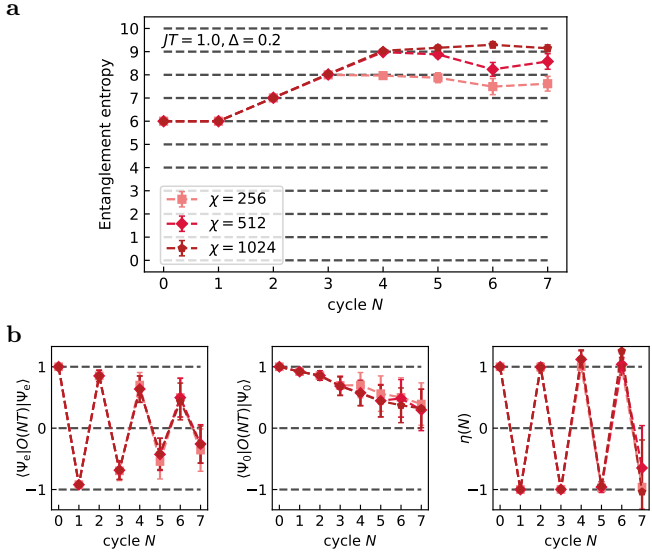


FIG. 22. MPS simulation of the  $e$ - $m$  transmutation away from integrability with  $JT = 1.0$  and  $\Delta = 0.2$ . The data is averaged over 20 disorder realizations, error bars denote the standard deviation. **a** The maximal entanglement entropy of all bonds at each time step in units of  $\log(2)$ . For visual clarity we only show the entanglement entropy for the simulation of the initial state with an  $e$  anyon, the results for the initial state without an  $e$  anyon are similar. **b** Left to right: The expectation value of the loop operator starting from a state with an  $e$  anyon, without an  $e$  anyon, and their ratio which gives the order parameter defined in Eq. (8).

it map to a time evolution of non-interacting fermions, which could also be simulated efficiently; thus, we need a simulation method like MPS that can deal with inter-

acting systems in general. Fig. 22a shows the maximal entanglement entropy of all bonds at each time step averaged over 20 disorder realizations, the error bars show the standard deviation. The different marker shapes and shades of red again denote the different bond dimensions used for the simulation. The plot of the entanglement entropy looks similar to before; only since now the state is no longer a stabilizer state, the entanglement entropy is no longer a perfect multiple of  $\log(2)$  and grows above  $S = 9\log(2)$  for the simulation with  $\chi = 1024$ . Fig. 21b shows the expectation value of the loop operator when starting from the state with an  $e$  anyon, when starting from the state without an  $e$  anyon, and their ratio which is the order parameter  $\eta(N)$  defined in Eq. (8). Since we are away from the fine-tuned point, we now see the expectation value of the loop operator decay in time both when starting from a state with an  $e$  anyon and without. This decay cancels approximately when taking their ratio, showing the oscillations of the order parameter between +1 and -1. The smaller bond dimensions show deviations from the  $\chi = 1024$  simulation, indicating that the simulation is not yet converged. The  $\chi = 512$  simulations still show deviations from  $\chi = 1024$  as early as four cycles in, indicating the need for a large bond dimension for the simulation. Note that the fact that the absolute value of the order parameter becomes larger than one at late times is not necessarily due to truncations in the MPS simulations, but can be an artifact of the finite system. Only in the thermodynamic limit do we expect the order parameter to perfectly oscillate between +1 and -1 away from the fine-tuned point.